ENHANCING GEOLOGIC INTERPRETATIONS WITH SEISMIC ATTRIBUTES IN THE GULF OF MEXICO

A Thesis Presented to the
Faculty of the Department of Earth and Atmospheric Sciences
University of Houston

In Partial Fulfillment
of the Requirements for the Degree

Master of Science

By

Scott H. Rubio

December, 2010

ENHANCING GEOLOGIC INTERPRETATIONS WITH

SEISMIC ATTRIBUTES IN THE GULF OF MEXICO

A Thesis for the Degree

Master of Science

By

Scott H. Rubio

Approved by Thesis Committee:

_____
Dr. Chris Liner, Chairperson

_____
Dr. Janok P. Bhattacharya, Committee Member

_____
Dr. Charles Winker, Outside Committee Member

_____
Dr. John Bear, Dean
College of Natural Science and Mathematics

December, 2010

ACKNOWLEDGEMENTS

I would like to thank my advisor Dr. Chris Liner for his direction and help in my research. I appreciate the countless time he has spent helping me solve problems and discussing my work. I would also like to thank Dr. Janok Bhattacharya for allowing me to work on this dataset and helping explain much of the geology. Thanks to Dr. Charles Winker for explaining the Plio-Pleistocene depositional systems, seismic characteristics, and recommending valuable resources. I would like to thank all of the other students involved with this dataset, (Grigoriy Perov, Patricia Lee, and Felipe Lozano), who helped out with software issues and explained the geologic systems. A special thanks goes to Patricia Lee for all her help. Thanks to Tom Doggett for all his time proofreading and correcting my writing.

I would like to sincerely thank Petroleum Geo-Services for providing this high-resolution 3D seismic dataset. I would also like to thank Schlumberger for providing the Petrel Interpretation software and Joel C. Patterson for ironing the licensing issues out. Many thanks go to TGS for allowing access to their well logs, Tony Delilla at FusionGeo for providing assistance with the ThinMan software and Dr. Fred Hilterman with Geokinetics for distributing digital well logs and check shots.

ENHANCING GEOLOGIC INTERPRETATIONS WITH

SEISMIC ATTRIBUTES IN THE GULF OF MEXICO

An Abstract of a Thesis

Presented to

the Faculty of the Department of Earth and Atmospheric Sciences

University of Houston

In Partial Fulfillment

of the Requirements for the Degree

Master of Science

By

Scott H. Rubio

December 2010

ABSTRACT

Seismic data interpretation is a primary method of viewing and mapping subsurface geologic features, making interpretation of structure and stratigraphy possible away from well control. The fundamental seismic data type is amplitude data, but seismic attributes (generated from amplitude) can reveal characteristics not easily seen in amplitude data itself. A 3D seismic survey is analyzed integrating seismic attributes. The study area lies above 2 seconds reflection time within the South Vermillion area of the Gulf of Mexico salt dome/mini-basin province, a local tectono-stratigraphic regime. Structure and stratigraphy in this area are controlled by salt tectonics, which aid in developing small mini-basins. Previous investigations used only seismic amplitude data to interpret growth-faulted delta sequences, slope channels, mass transport complexes, and other stratigraphic features in a mini-basin.

A re-examination of previous interpretations used seismic attributes, including coherence, curvature, and spectral inversion to improve geologic interpretation. Results validate the use of these attributes by improving slope channel and growth-faulted delta sequence interpretation. Incorporation of phase shift and well data improved depth and velocity measurements, and band pass filtering spectral inversion seismic enhanced resolvable limits.

TABLE OF CONTENTS

LIST OF FIGURES

LIST OF TABLES

INTRODUCTION

Seismic data interpretation is a primary method in viewing and mapping subsurface geologic features, making interpretation of structure and stratigraphy possible away from well control. The fundamental seismic data type is amplitude data, but seismic attributes (generated from amplitude) can reveal characteristics not easily seen in amplitude data itself. My study is an evaluation of three known seismic attributes detailing their abilities and limitations in highlighting geologic features.

Several students at the University of Houston have previously studied a 3D seismic volume from the Gulf of Mexico. Felipe Lozano characterized the upper 200 milliseconds of the data in his dissertation (Lozano, 2010, in progress), where he described wave-influenced strand plains. Grigoriy Perov and Patricia Lee have worked the western-most mini-basin in this data cube, located in the South Vermillion and Garden Banks Offshore Continental Shelf (OCS) blocks, where they observed and detailed the sequence stratigraphy, structural features, and origin of sediment.

The 3D seismic volume used by these students lies in the salt dome/mini-basin province, a highly complex area. The salt dome/mini-basin province Galloway (1975) described is found off-shore south-eastern Louisiana, in the Northern quadrant of the Gulf of Mexico. The sediments in this area date from the Pliocene/Pleistocene age, and are primarily deltaic in origin, embedded within

various salt structures (Winker, 1982). The salt structures account for much of the morphology in the area, including the development of a mini-basin environment.

Perov (2009) described fluvially-influenced delta lobes and slope channels. He explained 3D seismic data's ability to look within the stratigraphic features and compare the external morphology to the internal architecture of shelf-margin delta lobes. He then argued in favor of a fluvial dominated delta environment rather than wave or tide dominated delta environments. He also notes complex areas where seismic reflections are difficult to interpret.

Perov (2009) based his interpretation on seismic amplitude and some coherence horizon slices. The purpose of my study is to test Perov's interpretations of the mini-basin by applying seismic attributes such as coherency, curvature and spectral inversion. Seismic interpretation is subjective, so the focus of this study is not to refute Perov's interpretation, but test whether seismic attributes more clearly image key features of his interpretation. Seismic attributes may be able to identify geologic features that are obscure on amplitude data, such as stratigraphic boundaries, slope channels, or faults. My goal is to evaluate the three seismic attributes ability to clarify these geologic features.

STATEMENT OF PROBLEM

Previous investigations in a Gulf of Mexico shallow mini-basin have been based on seismic amplitude data and some use of the coherence attribute. Chaotic seismic character and low resolution in some key areas hindered these interpretations. This study analyzes seismic attributes in these difficult areas to improve our ability to image and interpret complex patterns representing complicated geological features such as stratigraphic boundaries, slope channels, and small scale faulting.

SETTING

Geologic Background

The study area (Figure 1) lies in the North-western portion of the Gulf of Mexico, which comprises early Quaternary deltaic sediments alongside much older Cenozoic salt deposits (Winker, 1982; Diegel et al., 1995). Extensive salt deposition along the continental shelf of the modern day Gulf of Mexico occurred during the Middle Jurassic (Ewing, 1958). Cenozoic deltaic deposits were deposited onto the continental margin. These sediments soon began accumulating as a result of the nearby Paleo-Mississippi fluvial system (Galloway et al., 2000; Suter and Berryhill, 1985; Ostermeier et al., 2002). Since Late Jurassic time, the basin has been a stable geologic province characterized by persistent subsidence of its central part, probably due at first to thermal cooling and later to sediment loading as the basin filled with thick prograding clastic wedges along its north-western and northern margins, particularly during the Cenozoic (Galloway et al., 2000). The result was an atypical basin setting where the salt subsidence created accommodation in the form of mini-basins. These smaller, chiefly circular basins formed in great numbers, super-imposed on the common large ocean basin, where deltaic deposits within these mini-basins commonly display listric growth faults. Furthermore, successive deltaic sequences comprise clinoforms, which are separated by flooding surfaces that

can be clearly seen in seismic data. Perov (2009) thoroughly described one such detection of a depositional system and its effect in this region.

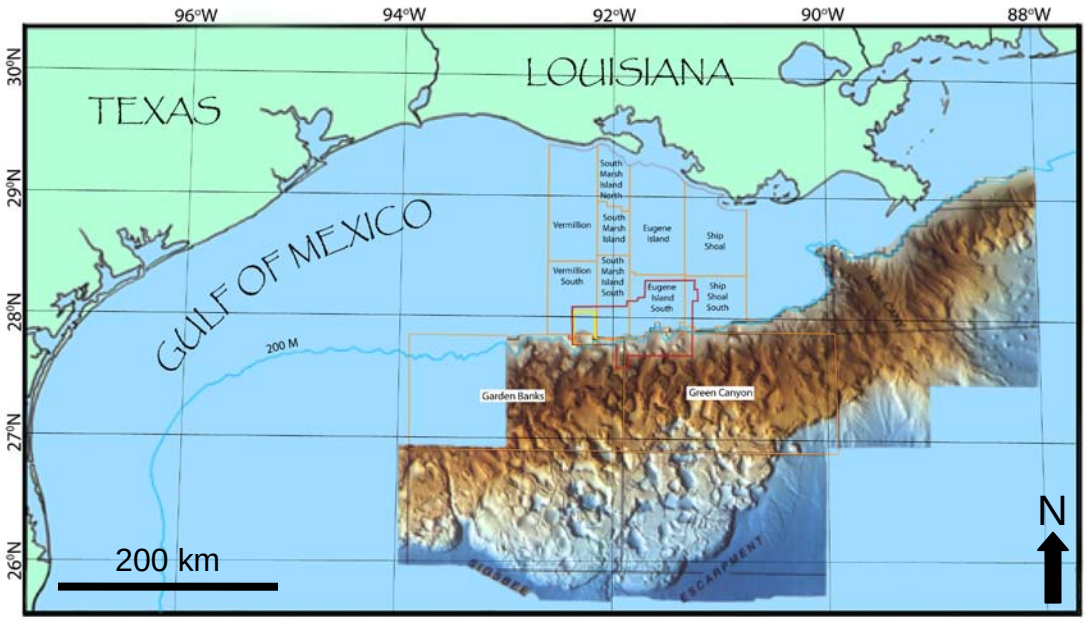

Figure 1: Regional map of the North-western portion of the Gulf of Mexico. Red box indicates seismic data cube used in this study and yellow box indicates the area of study. Regional bathymetry image is overlain as well as OCS blocks and 200 M water depth contour. (Portions taken from Diegel et al., 1995; Created with Patricia Lee)

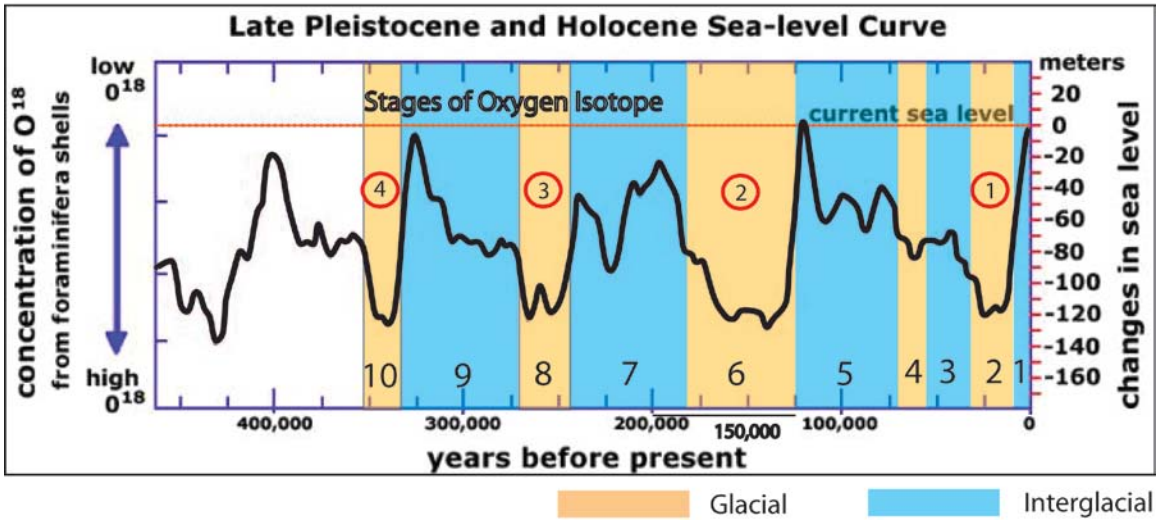

Figure 2: Eustatic sea-level curve showing sporadic advances during the Late Pleistocene and Holocene. Oxygen isotope stages 1 to 10 are shown with suggested timing of the deposition of the four Perov (2009) deltaic complexes. (Taken from Imbrie et al., 1984)

Tectonics and Stratigraphy

The area of interest lies in a complex tectono-stratigraphic regime called the salt-dome/mini-basin province (Galloway, 1975). The 600 km^2 mini-basin of interest contains two salt dome complexes that have been uplifted by overburden sedimentation. These salt massifs lie due west and due east of the mini-basin, confining the sediment deposition orientation from the northern direction. As a result of the properties of the upper mini-basin fill and the changes in thickness of the sediment successions against the flanks of the salt domes, Perov (2009) determined that the uplift of the western salt dome occurred before the rise of the eastern dome. There are notable extensional faults to the northeast and

northwest of the mini-basin; these large offset faults are clearly discernable in map view projections.

Perov's stratigraphy within the mini-basin comprises deltaic sequences of Late Pleistocene to Early Holocene age, which formed before and during the Oxygen isotope stage 6 eustatic sea level low stand between 180 and 125 ky (Figure 2) (Wellner et al., 2004; Fliedner et al., 2002). The deltaic sequences include undeformed to deformed chaotic complexes. This study focuses on the second deltaic complex in a succession of four. It displays clinoforms of different size, shape, and continuity obstructed by chaotic seismic reflections (Figure 3). The second deltaic sequence's deformation was interpreted to have multiple origins. Syn-depositional growth faults occurred as sedimentation continued, which is common in river-dominated deltas (Bhattacharya and Davies, 2004; Ewing, 1958; Diegel et al., 1995). The scale of faulting is relatively small and they are contained within 100 m thick seismic intervals. Mass transport complexes occur syn-depositionally; however, they are typically much larger features that occurred because of slope failure as the adjacent salt bodies uplifted.

Perov (2009) focused on the internal architecture of these delta deposits. This study continues along the same lines by trying to better define the internal architecture of the deltaic sequences in order to understand the morphology within this region. The improved imagery aids in locating faults and help determine if they are indeed growth-faults. These images also help detect slope channels and any other notable structural or stratigraphic features that are present within the mini-basin.

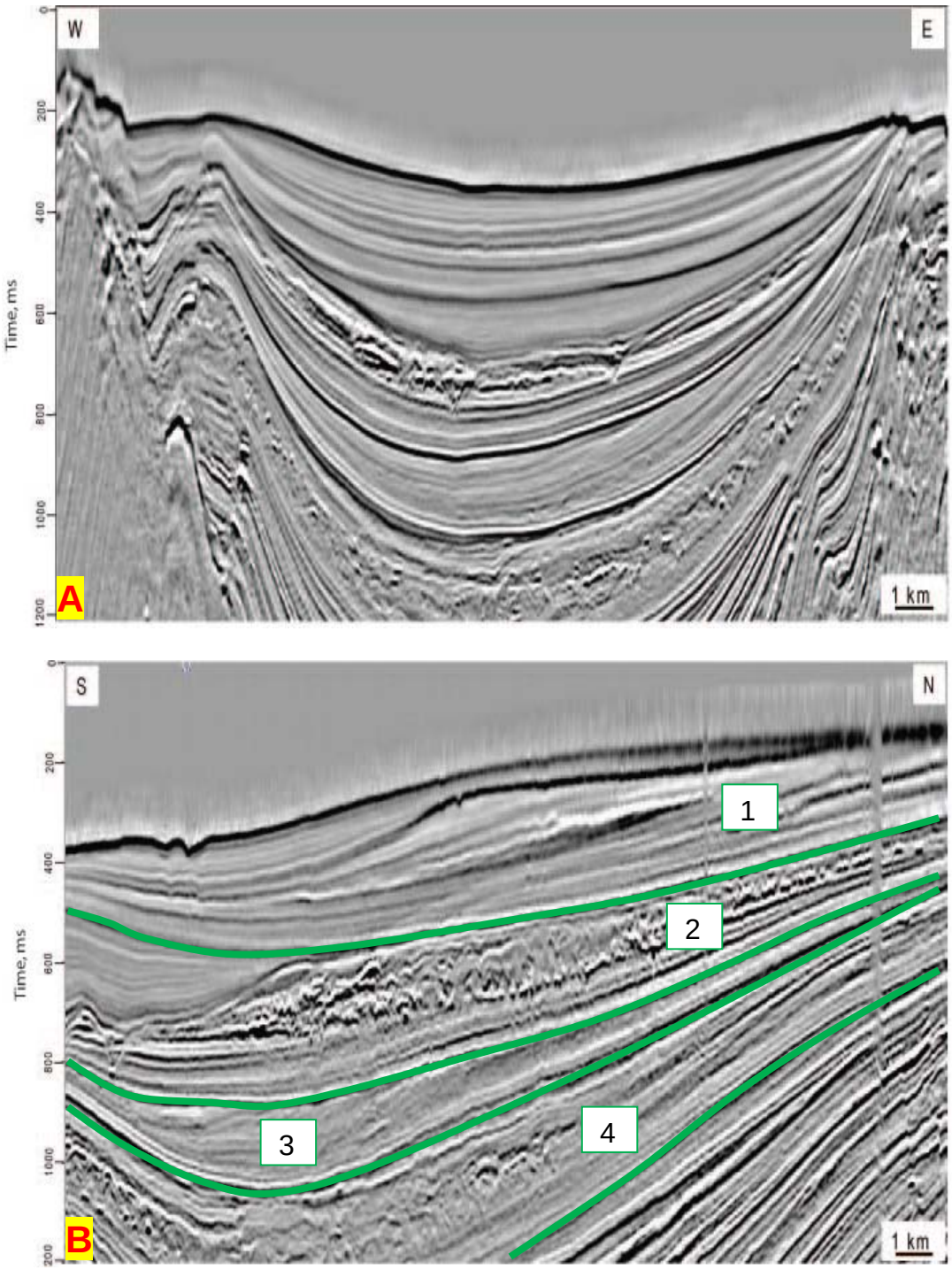
W
E
Time, ms
0
200
400
600
800
1000
1200
A
1 km
S
N
1
2
3
4
B
1 km

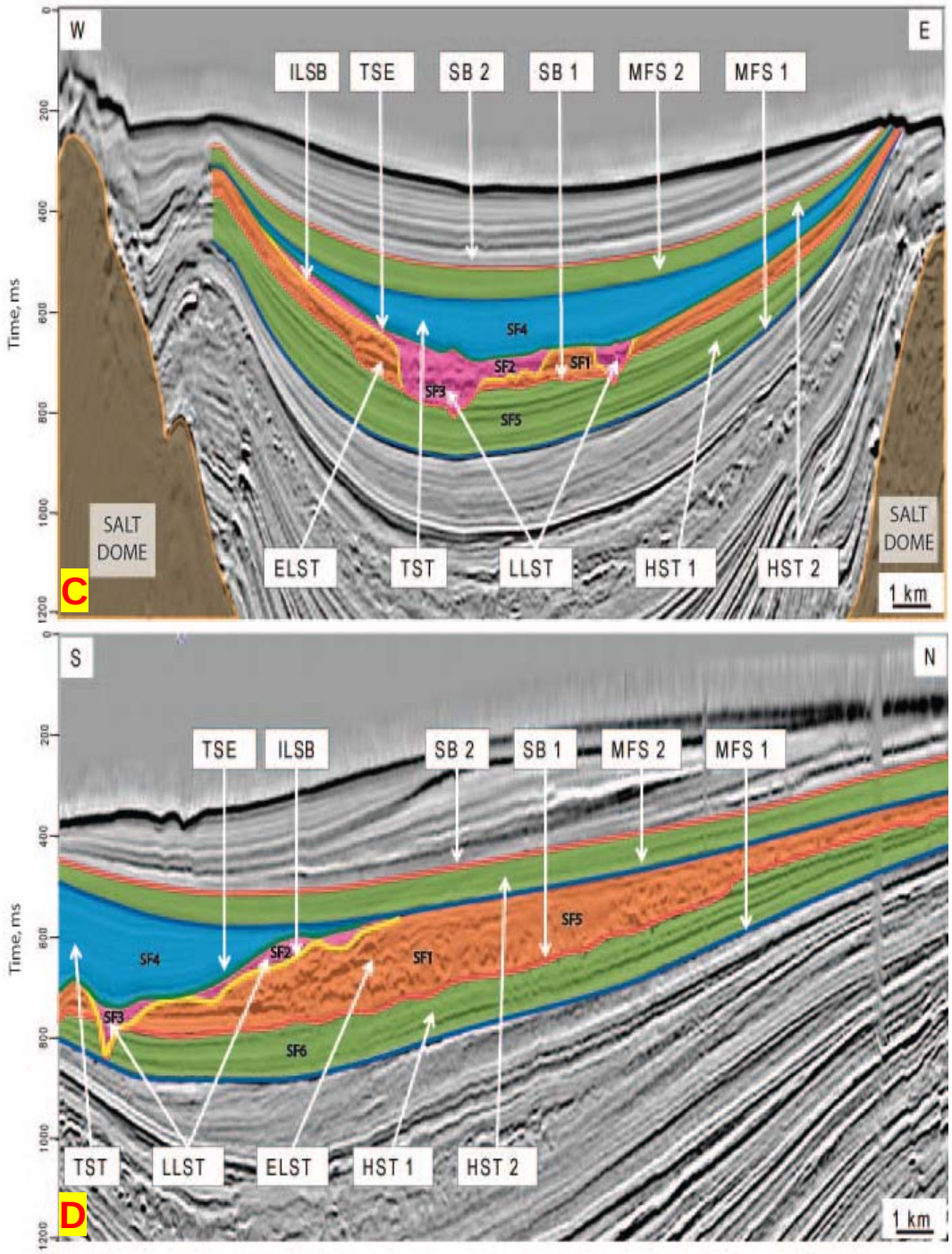

Figure 3: A) Strike view of the seismic volume. B) Dip view with labeled delta successions. C) Strike view with Perov's (2nd delta succession) seismic sequences colored and labeled. D) Dip view with Perov's (2nd delta succession) seismic sequences colored and labeled.

SEISMIC ATTRIBUTES

Introduction

Liner (2004) defines seismic attributes as specific quantities of geometric, kinematic, dynamic, or statistical features derived from seismic data. In 2004, there were over 220 reported seismic attributes and there are even more today. A valuable seismic attribute is one that enhances geologic features including structural features like faults, or depositional and stratigraphic elements such as channels and lobes (Chopra and Marfurt, 2005).

It is important to select seismic attributes that will be most useful in exhibiting the features of interest in a specific seismic dataset. For this reason, one must be familiar with all aspects of the data (i.e. dip, azimuth, acquisition parameters) and geologic setting, in order to select the attributes that are likely to work best. Perhaps the most widely used attribute is coherence because of its fault detection ability (Chopra and Marfurt, 2006). Another widely used attribute is curvature, which is a recent addition to the seismic attribute world. Curvature focuses on characterizing structural geometry (Sigismondi and Soldo, 2003). Spectral inversion is a type of enhanced imaging attributes. It provides another view of the data with increased resolution. The following section explains development of these attributes and their application to this study.

Coherence

Coherence is an edge detection attribute that highlights geologic features that have abrupt boundaries. Due to its ability to image discontinuities, coherence is applicable to many types of structural and stratigraphic events (Figure 4). Bahorich and Farmer (1995) describe the coherence seismic attribute as a measure and representation of the trace-to-trace similarities of seismic reflections. Depending on a trace's neighbouring waveform and amplitude likeness in the in-line or cross-line directions, the algorithm attempts to predict a center trace value using an N-trace operator. If the central trace value is predictable, the area is coherent and a low value is output, where the area is incoherent or the central trace value is not predictable, a high value is inserted. The result is a dataset where non-predictable values are highlighted against a continuous background. Therefore, the display identifies faults, fractures, channels, and other sharp-edged stratigraphic features, because of the lateral changes in seismic traces that occur at these discontinuities (Chopra, 2002; Marfurt et al., 1998).

Many studies demonstrate this attribute is capable of pinpointing faults, fractures, channels, and other types of geologic features (Bahorich and Farmer, 1995; Chopra, 2002; Chopra and Marfurt, 2005; Chopra and Marfurt, 2006). For this reason, the use of coherence in this study examines the previous interpretations of channels and slumps in this mini-basin. Perov (2009) incorporated this attribute in portions of his interpretation. My study differs from Perov by using this attribute in an angled orientation as well as using different

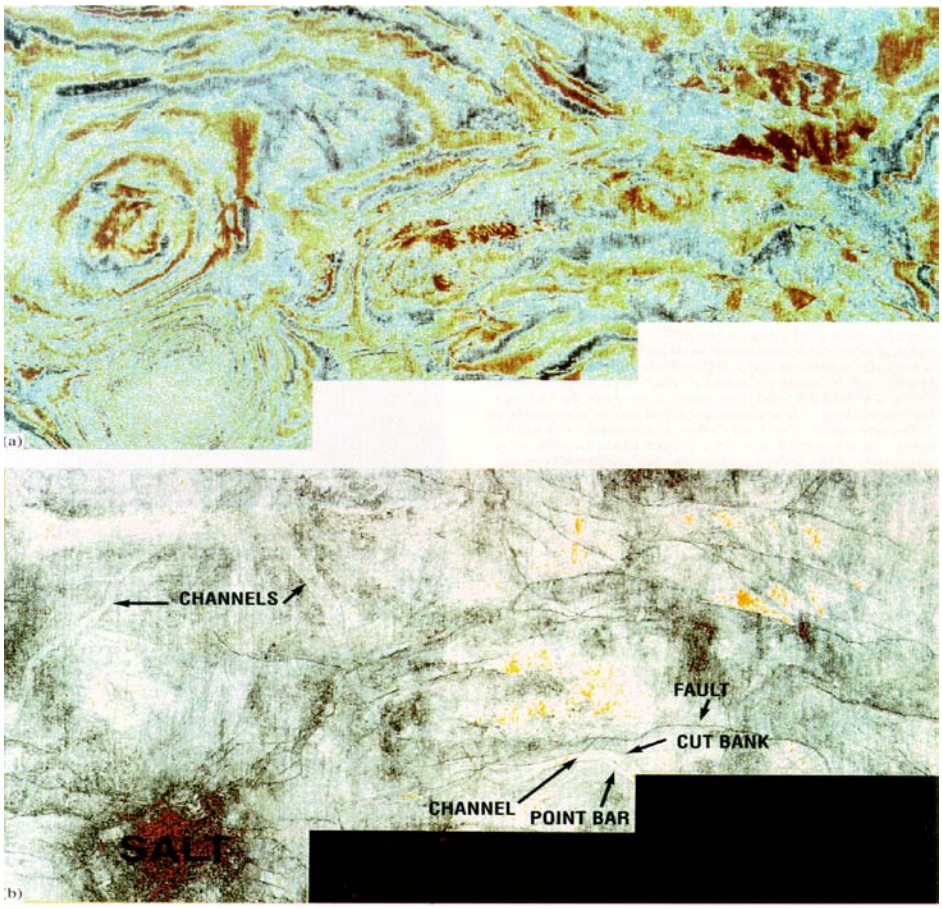

Figure 4: Early coherence calculation depicting the ease in the interpretation of faults and channels. (Taken from Bahorich and Farmer, 1995)

coherence parameters to improve imaging. The clearer images provided by this attribute show improved imaging of faults, slumps, and slope channels.

Curvature

The curvature attribute is similar to the coherence attribute. It reveals many of the same geologic features, but it differs because it focuses on the geometric aspects of reflectors (Chopra and Marfurt, 2006). Stewart and Podoloski (1998) were of the first to apply curvature analysis to seismic surfaces

computing local slopes and estimating 3D shape. Where features occur, their presence is recorded in multiple seismic traces. By linking seismic reflections on these traces, a regional dip and azimuth is determined. The newly created dataset consists of values indicating to what degree certain areas deviate from being planar (Roberts, 2001; Sigismondi and Soldo, 2003). The result is a three-dimensional attribute that highlights seismic reflections of zero, positive, and negative curvature (Figure 5). Because this attribute removes regional dip, it enables the emphasis of smaller-scale features like faults, fractures, flexures, and folds (Roberts, 2001; Al-Dossary and Marfurt, 2006; Chopra and Marfurt, 2008). This study uses curvature to help identify previously interpreted geologic features such as growth faults.

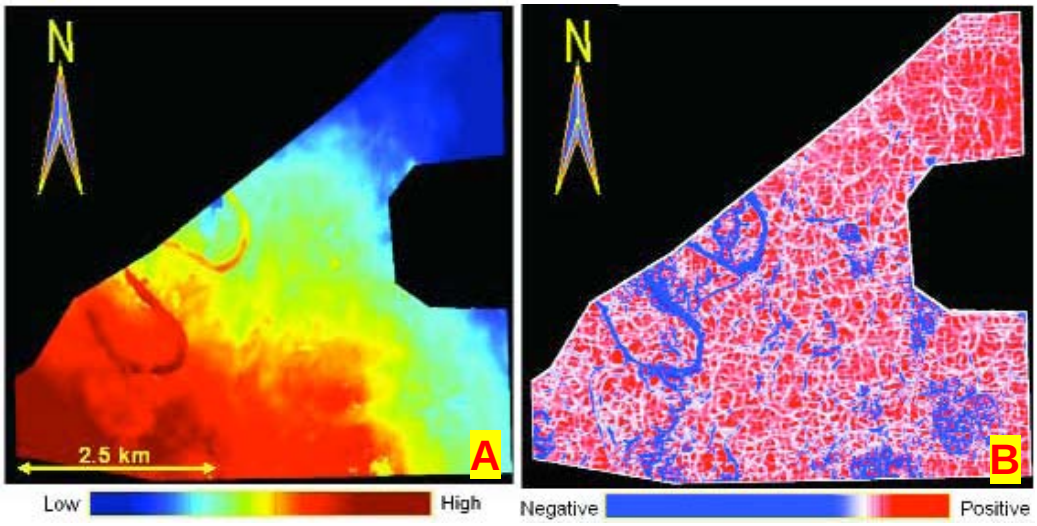

Figure 5: A) Time slice through amplitude data. B) Most-positive curvature better displaying the channel extents and illuminating other channels in blue. (Taken from Chopra and Marfurt, 2006)

Spectral Inversion

Spectral inversion follows the basic principles of an inverse problem, where a set of parameters are used in a simulation to create model data that is compared to observed data. The difference between model and observed data is used to update simulation parameters to achieve a better fit. This process is continued until the model data matches the observed data within specified tolerance. Spectral inversion (Puryear and Castagna, 2008) estimates reflection coefficients from seismic traces by decomposing the coefficients into positive/negative dipoles. The inversion process then generates relative impedance layers that conform to the measured reflection coefficients. This process creates two attribute datasets, one displaying the reflectivity series and one displaying the impedance layers. By subtracting insignificant seismic reflectors, this method is able to image geologic features well below the tuning thickness and improve imaging of subtle stratigraphic features. Therefore, this process actually increases the resolution of the dataset. Fusion ThinMan spectral inversion software is used in this study as the enhanced imaging tool (Figure 6). The reflectivity series seismic attribute is used to identify faulting in cross-section that would be unresolved on seismic amplitude alone.

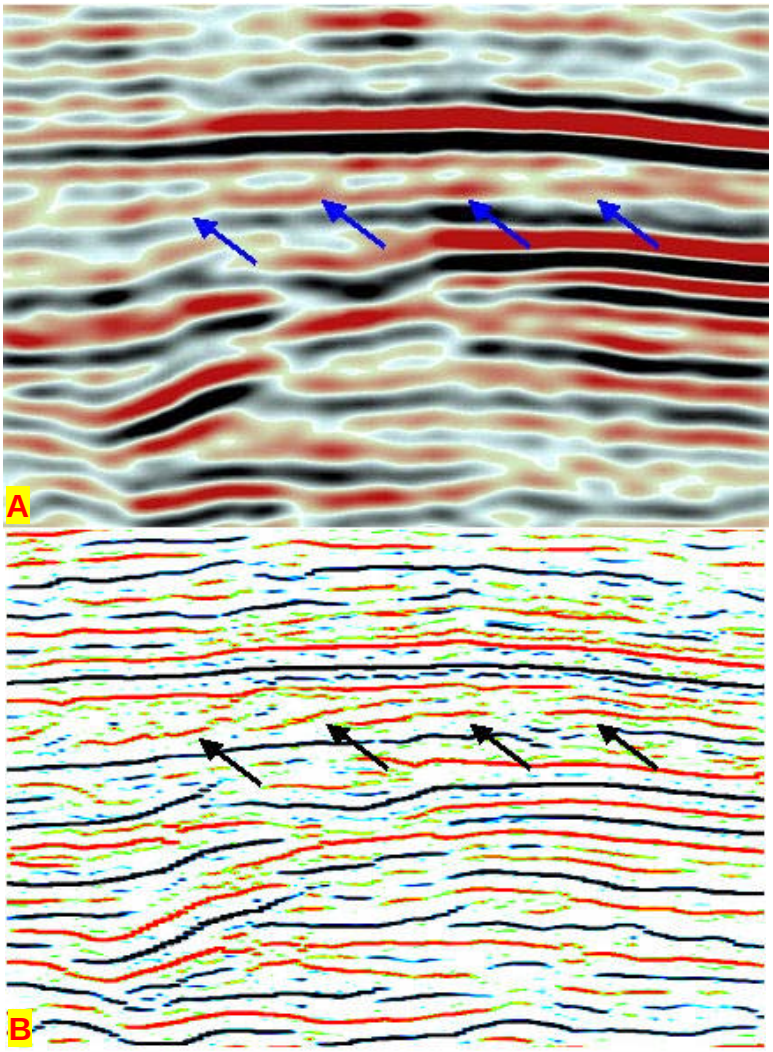

Figure 6: A) A seismic amplitude dataset from the Gulf of Mexico where arrows point to a chaotic interval. B) ThinMan reflectivity series seismic dataset where arrows point to same interval clearly showing progradational sands. (From www.fusiongeo.com)

METHODOLOGY

Data Description

This study uses a high-resolution 3D seismic dataset donated by Petroleum Geo-Services that lies in the salt dome/mini-basin province in the Gulf of Mexico. The data is located about 185 kilometers south of the Louisiana coast (Figure 1), and covers an area of 8000 km^2 (288 Offshore Continental Shelf (OCS) blocks). The study area is a smaller area (31 OCS blocks) including the westernmost mini-basin. This trimmed area lies entirely in the Vermillion South Addition and Garden Banks fields between latitudes 27^o 51' N – 28^o 4' N and longitudes 92^o 11' W – 92^o 23' W. The in-line and cross-line lengths are about 24,750 m and 19,125 m.

The seismic data was obtained via towed streamer acquisition using two sources and three receiver cables with a maximum offset of 6000 meters. There were 240 channels per streamer with a 25 meter group interval and a CMP bin dimension of 25 meters x 37.5 meters. The data has a fold of 48, 10.5 second record length, and a 4 millisecond time sample rate. The time interval used in this study is 0 to 1.5 seconds. The data was processed using a 3D Kirchhoff bending-ray pre-stack time migration.

This seismic amplitude data is interpreted in Schlumberger Petrel 2010 software, along with coherence, curvature, and spectral inversion reflectivity series. The spectral inversion data was created outside of the Petrel 2010

software using Fusion ThinMan software; however, it was reviewed and analyzed in the Petrel 2010 software.

A frequency spectrum from seismic amplitude data (Figure 7) was generated using a seismic unix script (Figure 8) to show the bandwidth of four traces located at in-line 23362-23364 and cross-line 986-987 on the time interval 500-750 ms. Average interval velocity is 1672 m/s, determined by time-depth curves and well data provided by F. Hilterman (2010). The spectrum ranges from 5 – 60 Hertz, giving a dominant frequency of 27.5 Hz. Thus, the local wavelength is 61 m, vertical resolution 15 m, inline horizontal resolution 30 m, and crossline horizontal resolution 37.5 m.

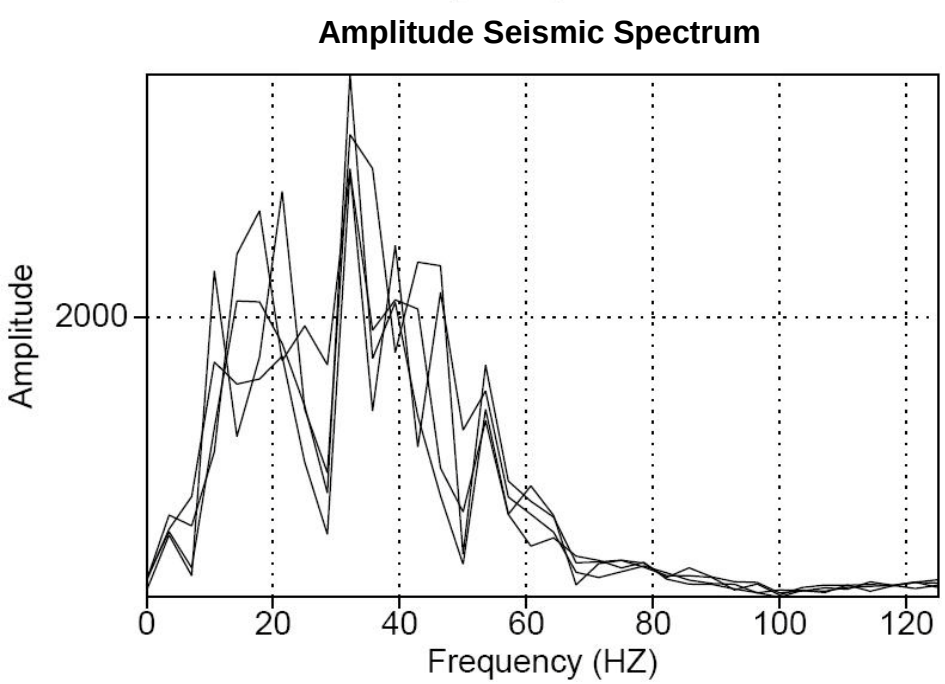

Figure 7: Frequency spectrum of amplitude data on 500 – 750 ms interval. Most energy is concentrated between 5 and 60 Hz. Dominant frequency is 27.5 Hz with a strong peak at 35 Hz. Nyquist frequency (125 Hz) is the upper limit on the x-axis.

```
segyread tape=./Dataset.segy > trace.su

sufft < trace.su | suamp | supsgraph style=normal title=Spectrum
label1="Frequency (HZ)" label2="Amplitude" hbox=4 grid1=dot grid2=dot
> spectrum.ps

ps2pdf spectrum.ps
```

Figure 8: Seismic Unix frequency spectrum plot script. (Provided by Chris Liner, U of H, Personal Communication, 2010)

Six well logs and check shots were provided by Geokinetics for this study (Table 1). Well log types include depth, gamma ray, neutron porosity sandstone, density, resistivity, sonic, sand %, and hole effects. These logs were uploaded into Petrel and used to develop time-depth relationships, estimate interval velocities, extract wavelets, and determine seismic signal phase.

Table 1: Geokinetic's donated well logs and check shots used in this study.						
Well Name	**Latitude**	**Longitude**	**API/Check shot**	**Kelly**	**Log Start**	**Log Stop**
(4) OCS G-2583 NO.2	28° 1' 32" N	92° 22' 5" W	177064020000	26.82 m	304.8 m	2834.9 m
(4480) OCS G-6685 NO.1	27° 56' 49" N	92° 21' 2" W	177064057800	24.99 m	487.7 m	2834.6 m
(5319) OCS G-2584 NO.1	28° 2' 6" N	92° 13' 32" W	177064012800	20.73 m	274.3 m	1950.7 m
(5387) OCS G-3141 NO.3	28° 0' 40" N	92° 15' 37" W	177064039800	27.43 m	487.7 m	3779.5 m
(6547) OCS G-3141 NO.2	28° 1' 23" N	92° 15' 10" W	177064025600	12.8 m	335.3 m	2987.0 m
(6549) OCS G-2580 NO. 1	28° 4' 4" N	92° 15' 40" W	177064014600	28.5 m	304.8 m	2590.8 m

Procedure

Previous interpretations have been made concerning the depositional environment of the westernmost mini-basin in the Petroleum Geo-Services seismic dataset (Perov, 2009). This work was the starting point of my interpretation of faults, horizons, channels, and boundaries. I used Perov's interpretation to locate areas of high interest, including heavily growth faulted intervals, mass transport complexes, and slope channels. Seismic sections of these features were extracted from the data for seismic attribute analysis.

These seismic sections were analyzed by taking the clearest seismic image then interpreting the location of the feature. Well and check shot data was used to zero phase the data and determine interval velocities. Seismic attributes (coherence, curvature, and spectral inversion) were viewed in time slice, horizon slice, and vertical sections. These map views included 3D projections of surfaces such as maximum flooding surfaces, sequence boundaries, transgressive surfaces of erosion, and 2D time slices. Surfaces, individual cross sections, and images from identical locations were also transferred from Perov (2009) to show additional standout that was either missed or un-interpretable in amplitude data alone. When the seismic attributes are draped to these map views and cross sections, they create complimentary seismic images for use with amplitude data.

All attributes involve user-specified input parameters. Coherence and curvature are both in the suite of volume attributes provided by the Petrel 2010 software. Coherence has three parameters, inline range, crossline range, and vertical smoothing. Vertical smoothing was set to 5 (very low), inline range was

set to 3, and crossline range was set to 1. Curvature settings (and my values) include method (most positive curvature), interpolation method (spline), vertical radius (7), inline/crossline radius (1), and correlation weighting (cosine squared). Fusion ThinMan spectral inversion software requires two window length parameters and a smoothing parameter called alpha. The best results used window lengths of 120 ms and 5 ms and alpha of 5. By manipulating color bars and contrast, the seismic attributes enhanced distinct features in cross section and map view. These parameter and display choices provided attributes that improved geologic interpretation.

RESULTS

Geophysical Processing

Well control (Table 1) was used to extract the wavelet in the intervals of interest discussed in Perov (2009). These intervals (Figure 3) were tracked back to the nearest well (number (6547) OCS G-3141 No.2). The seismic wavelet was then extracted using an automatic match process. The results (Figure 9) show that the phase of the wavelet is 15.3^{o}. In order to correct for the phase of the wavelet, a phase shift of 15^{o} was applied to the 3D data, producing a seismic volume with a phase mismatch relative to well control of less than 1^{o}. With the corrected phase, correlation of seismic reflections becomes more accurate in both time and depth.

Check shots provide velocity measurements that differ from the 1550 m/s estimated by Wellner et al. (2004) and used by Perov (2009). Check shot data implies a higher velocity of 1672 m/s and this is used throughout the current study. This velocity difference of nearly 8% affects all depth calculations provided in Perov (2009), as well as wavelength and resolution.

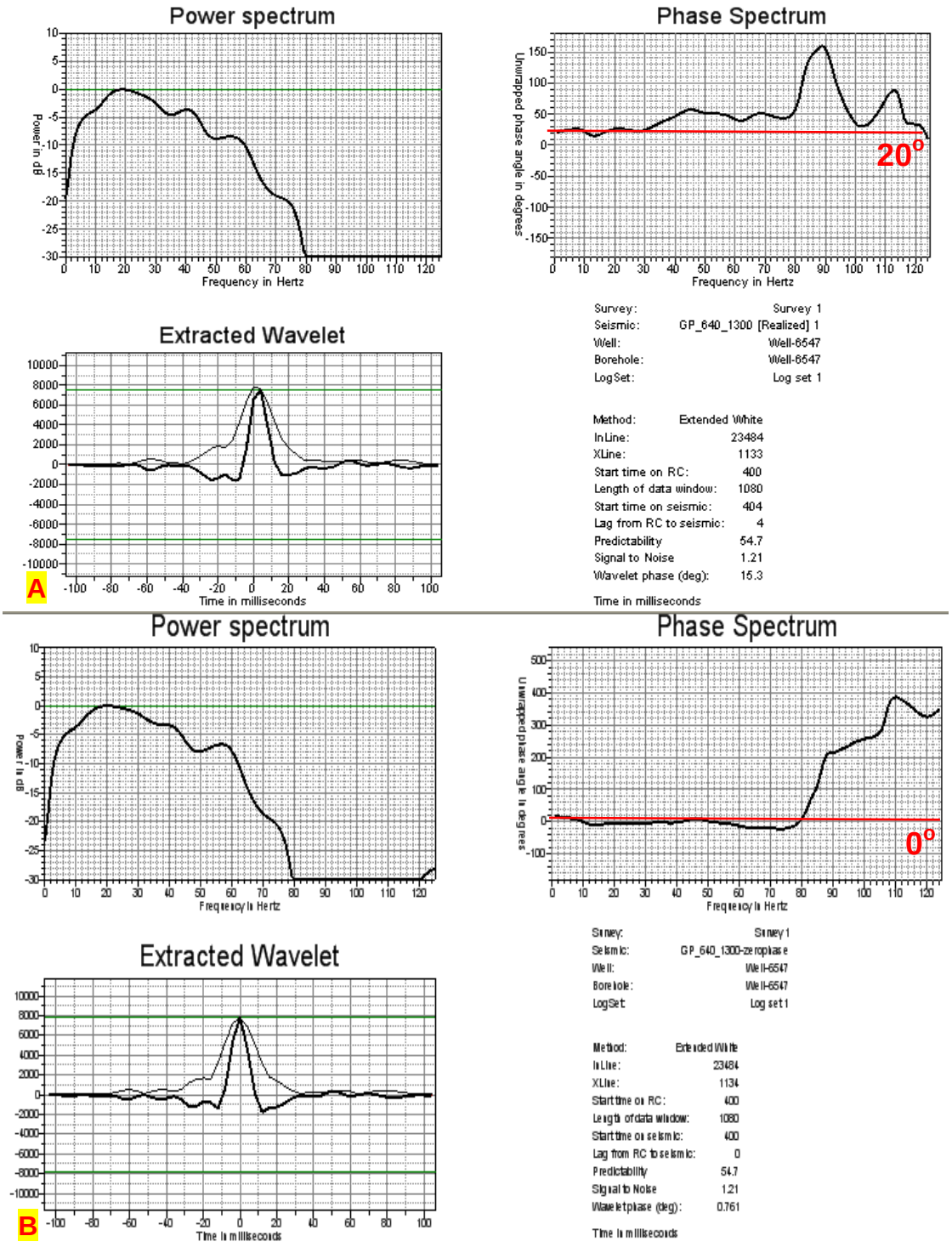

Figure 9: A) The extracted wavelet phase spectrum from the seismic data shows a 15.3^{o} phase. B) The corrected seismic data now shows a 0.761^{o} phase as well as a more symmetrical wavelet.

Resolution Improvement

Bandwidth of spectral inversion (SI) can be compared to that of seismic amplitude data using a cropped seismic section lying within a chaotic seismic interval (Inline 23362-23364; Crossline 986-987; Time 500-750 ms), see Figure 10. This location was used because Perov (2009) determined that this interval was of high interest due to the stratigraphic and structural complexity. Imaging of the number, dimension, and amount of throw on these faults along with the location of the décollement surface are all aspects of this interval that may be improved with wider seismic bandwidth.

Again, using the Seismic Unix script in Figure 8, the frequency spectrum of the SI data is computed and shown in Figure 11A. For SI calculation, the amplitude data was resampled from 4 ms to 1 ms. SI reflectivity frequency spectrum shows energy between 10 – 500 Hz with a dominant frequency of 245 Hz. The corresponding wavelength is 7 m, vertical resolution 2 m, inline horizontal resolution 30 m, and crossline horizontal resolution 37.5 m. The horizontal resolution will remain constant despite the applied attribute as the acquisition bin dimensions do not change. Compared to amplitude data, the SI data has nearly 1/8 of the wavelength and vertical resolution.

The SI impedance frequency spectrum shown in Figure 11B has energy between 10 - 150 Hz with a dominant frequency of 70 Hz. The wavelength is 24 m, vertical resolution 6 m, inline horizontal resolution 30 m, and crossline horizontal resolution 37.5 m. Compared to amplitude data, the SI impedance data has just over 1/2 of the wavelength and vertical resolution.

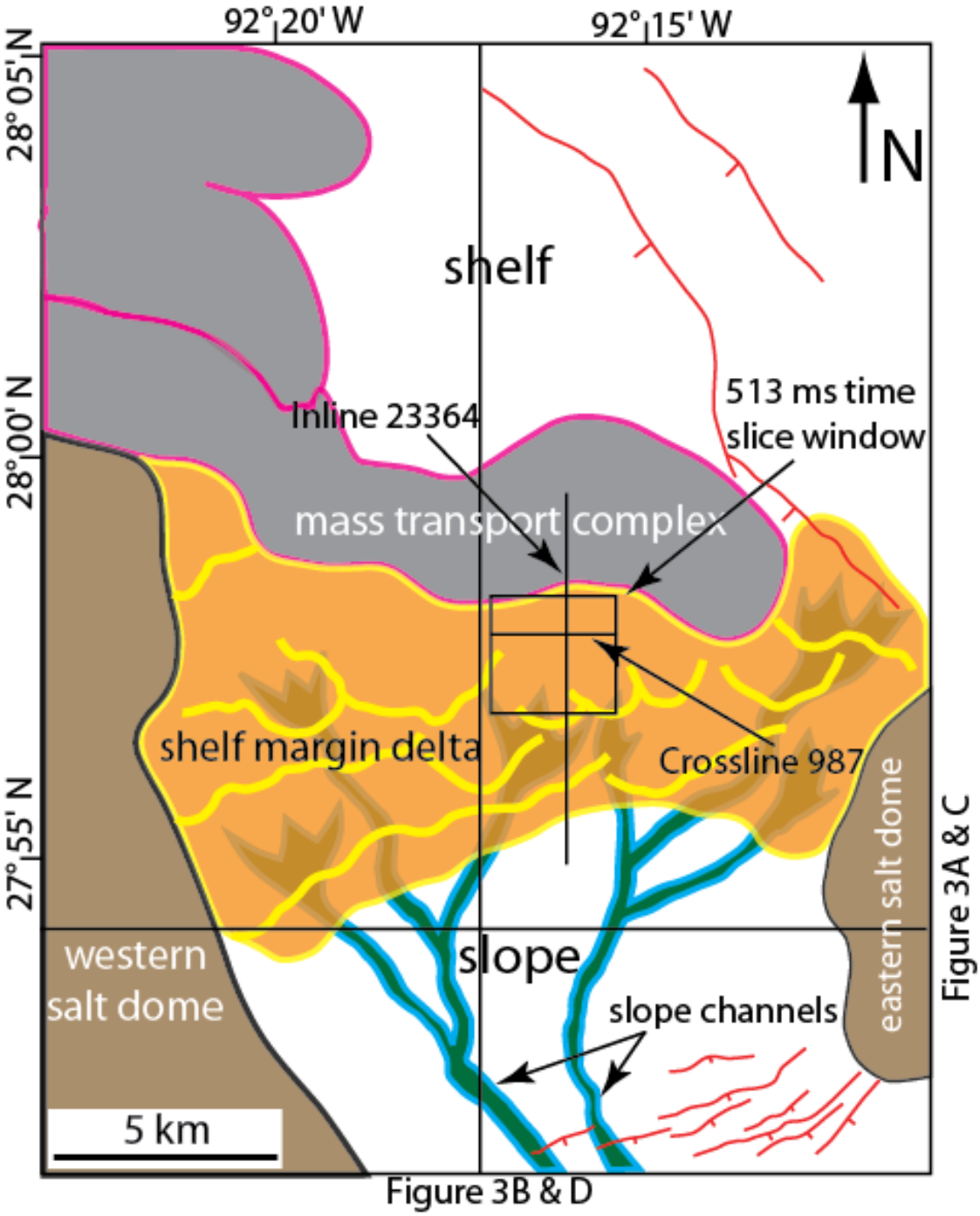

Figure 10: Schematic paleogeologic map of the study area. Note the location of seismic cross-sections shown in black lines. (Modified from Perov, 2009)

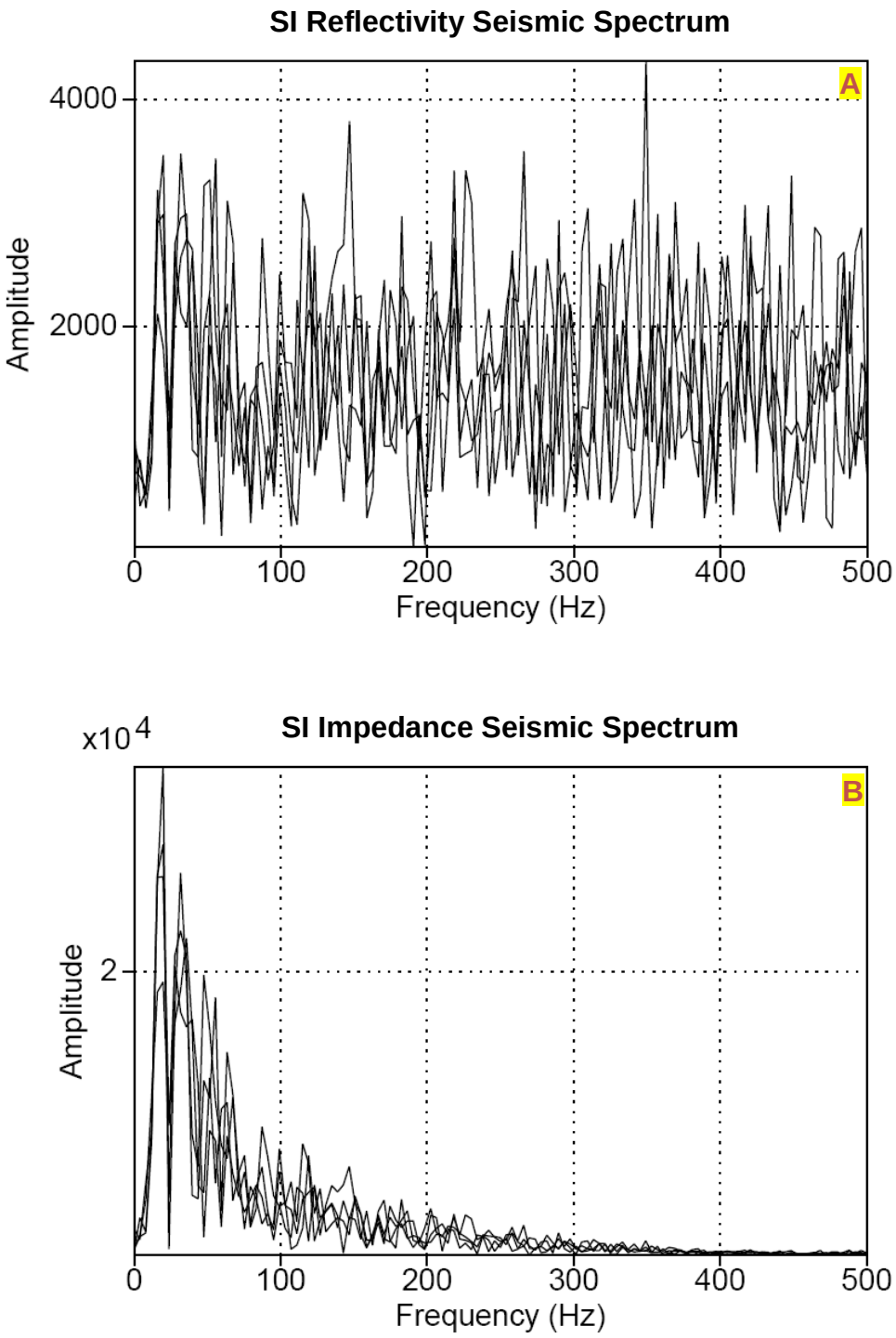

Figure 11: A) Frequency spectrum of SI reflectivity. Most energy is concentrated between 10 and 500 Hz with a strong peak at 350 Hz. B) Frequency spectrum of SI impedance seismic. Most energy is concentrated between 10 and 150 Hz with a strong peak at 20 Hz. Nyquist frequqency (500 Hz) is the upper limit on the x-axis.

Trace extraction from the amplitude and SI datasets (Figure 12) also produce similar results. I used identical traces in both datasets to perform the trace extraction at Inline 22470 and Crosslines 640-649. SI results show an increase in resolvable seismic reflections, heightening resolution within the seismic intervals. Differences in seismic are shown in Figure 13.

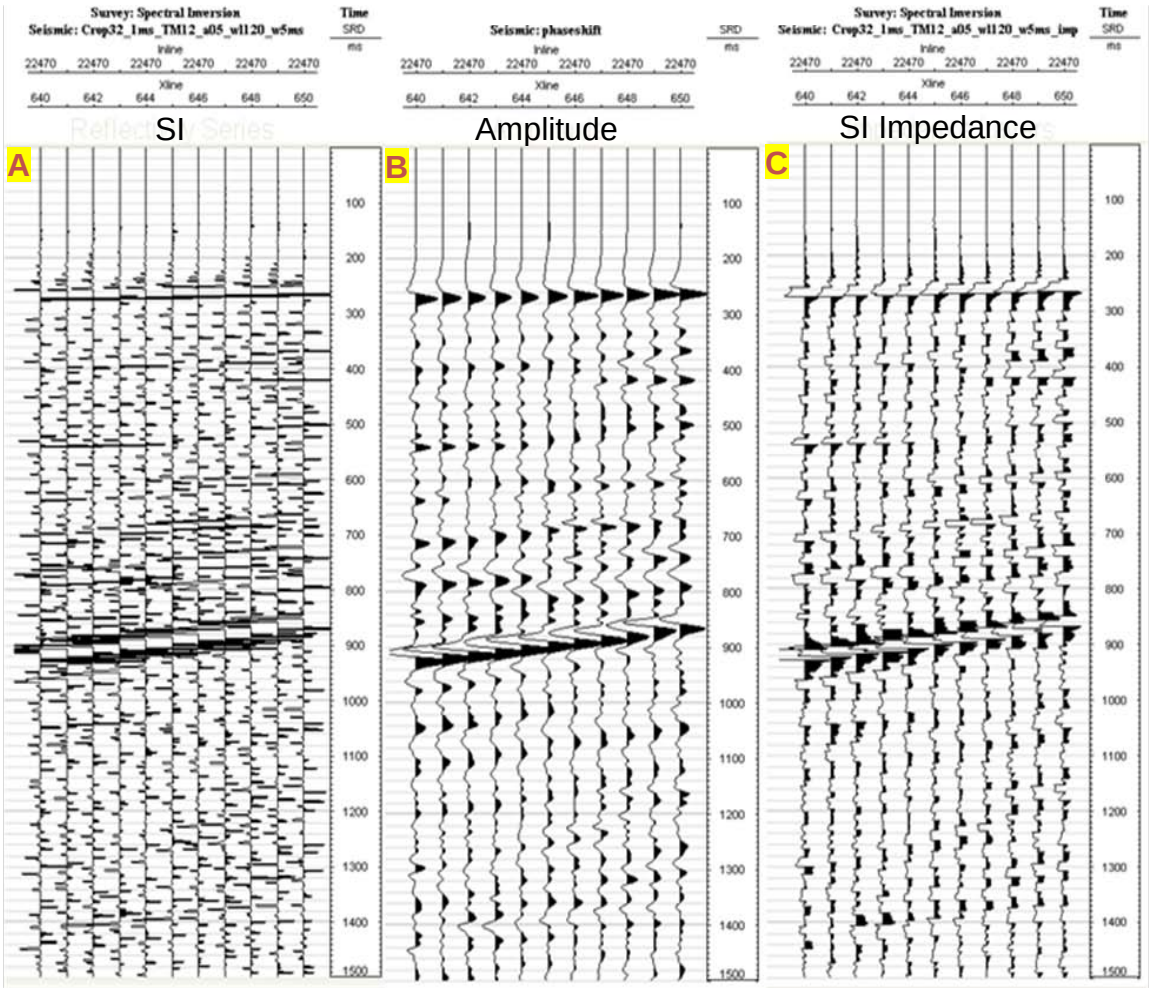

Figure 12: A) Trace extraction from SI seismic. B) Trace extraction from amplitude seismic that Perov (2009) used for interpretation. C) Trace extraction from the SI impedance seismic, note the blocky appearance expected of impedance inversion.

Attribute Analysis

The previously mentioned chaotic area is interpreted by Perov (2009) to be heavily faulted. With application of spectral inversion to this seismic interval, it became clear that Perov's interpretation was accurate in describing the deformation type; however, the improved images altered correlation of seismic reflections and fault locations.

Figure 13 shows the chaotic area (crossline 987) in cross-section. Amplitude seismic in Figure 13A has very few continuous beds and many unresolved seismic reflections. Full bandwidth SI seismic in Figure 13B displays discontinuous seismic reflections, but the upper clinoforms are more sharply defined. SI impedance seismic in Figure 13C shows discontinuous seismic reflections, and a blocky appearance that makes it hard to interpret as well. Amplitude seismic shows many circular features with a mixture of faint and bright reflectors. SI tones the bright reflectors down and resolves circular feature boundaries, but they are more discontinuous. These results show that SI impedance is too difficult to interpret for my data and, therefore, it is excluded from any further use in this study. Full bandwidth SI seismic improves resolution but does not correlate easily with seismic amplitude reflections. To enhance interpretation of SI data, a band pass filter is applied to improve continuity.

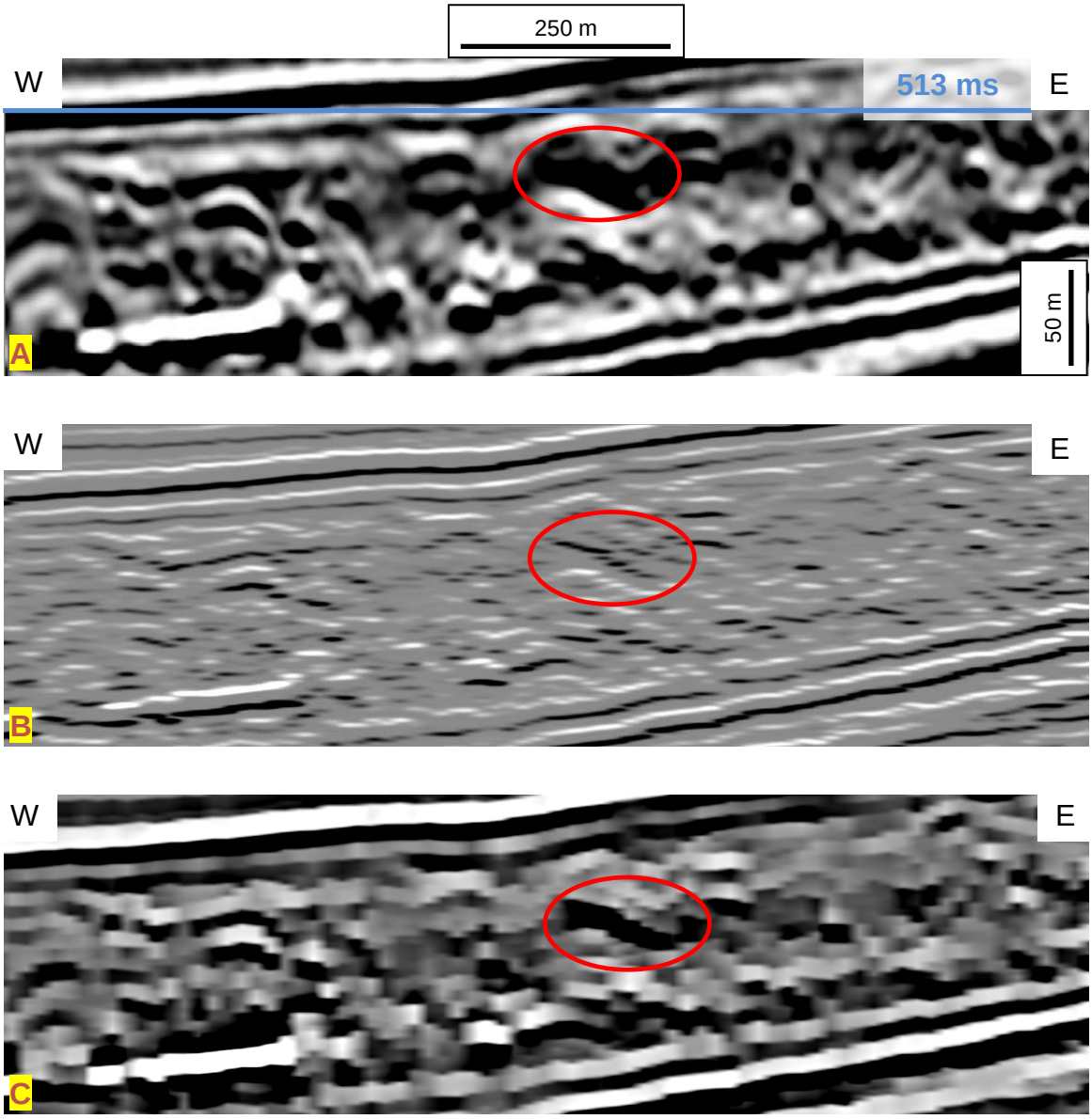

Figure 13: A) Crossline 987 in amplitude seismic, note unresolved seismic reflections in red circle. B) Crossline 987 in SI seismic, note discontinuous seismic reflections in red circle. C) Crossline 987 in SI impedance seismic, note blocky appearance in red circle.

Figure 14 compares seismic amplitude data (Figure 14A) to SI with 10 - 70 Hz band pass filter (Figure 14B), a 10 - 90 Hz filter (Figure 14C), and a 10 - 110 Hz filter (Figure 14D). Comparison of these results shows a better trace-to-trace continuity of beds in the SI seismic as well as resolution of many reflectors unseen on amplitude. Higher resolution is achieved with a broader band pass filter frequency range, unfortunately lower trace-to-trace continuity occurs at a broader range as well. Therefore, Figure 14C (SI seismic with 10 - 90 Hz band pass filter) is the best seismic image to use for interpretation as it strikes a balance between these effects.

The band pass filter makes it evident that spatial aliasing is a problem that is degrading resolution and interpretability in this seismic interval as well as the entire dataset. Spatial aliasing is a result of moveout between adjacent traces being greater than half the dominant period of the wavelet (Liner, 2004). Figure 14 has a vertical exaggeration of 8:1 with less than 1^{o} dipping clinoforms above and below a 3^{o} dipping faulted interval. This complex interval has internal dipping features on the order of 40^{o}. These steep features are degraded as a result of spatial aliasing, which displays false dips by correlating traces from different seismic events. SI generates higher frequency data from the seismic that is progressively more spatially aliased. The maximum seismic amplitude unaliased dip within this crossline interval (Figure 14A) is 14^{o} and the maximum SI unaliased dip within this crossline interval (Figure 14B,C,D) is 9^{o}.

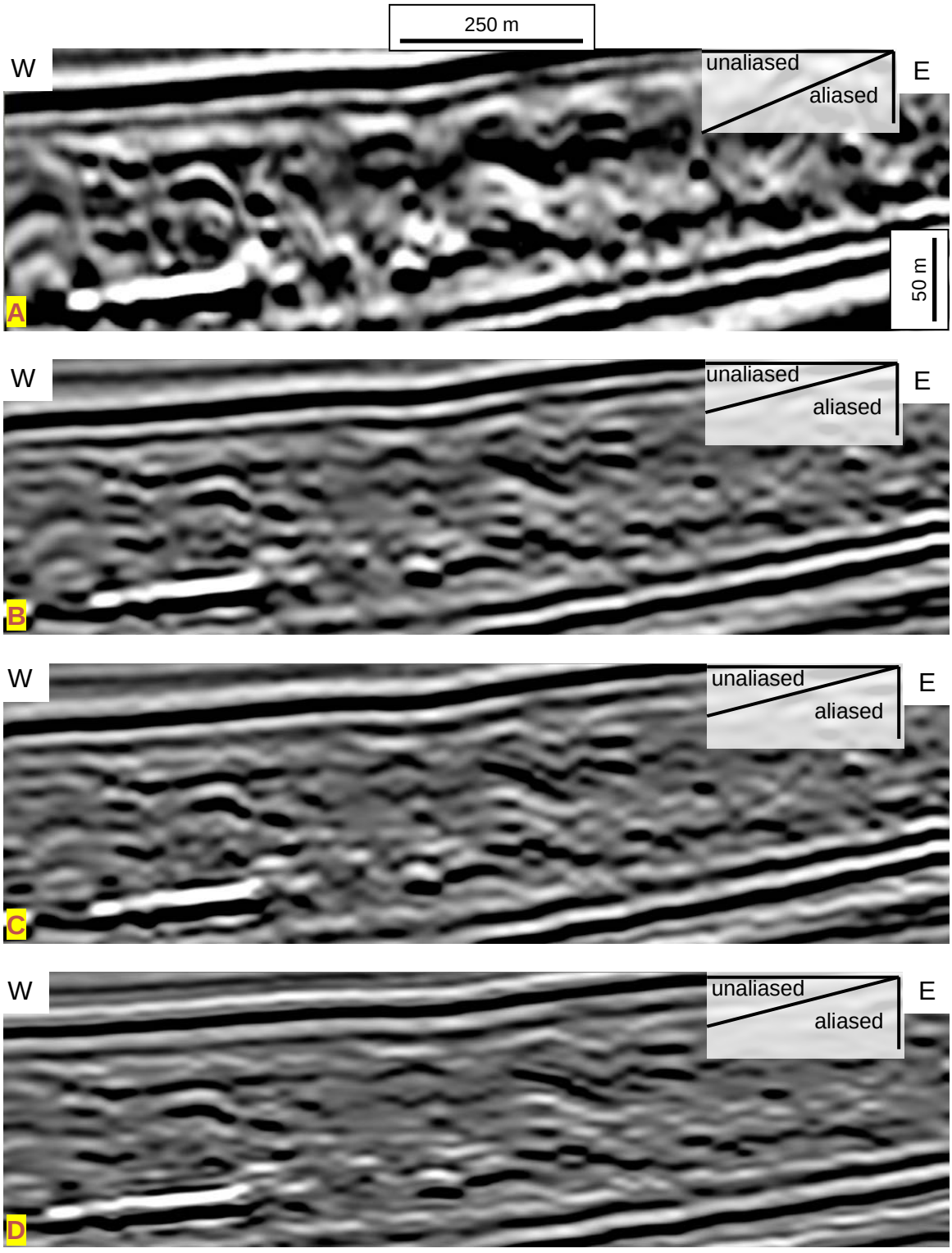

Figure 14: A) Crossline 987 seismic amplitude. B) Crossline 987 SI seismic with 10-70 Hz band pass filter. C) Crossline 987 SI seismic with 10-90 Hz band pass filter. D) Crossline 987 SI seismic with 10-110 Hz band pass filter. Vertical exaggeration is 8:1, max amplitude unaliased dip is 14^{o}, max SI unaliased dip is 9^{o}, and dip protractor shows aliased and unaliased dips.

The seismic unix script (Figure 8) is used again to generate the frequency spectrum of the SI seismic with 10 - 90 Hz band pass filter. The resulting frequency spectrum shown in Figure 15 has energy between 10 - 90 Hz with a dominant frequency of 40 Hz. The wavelength is 42 m, vertical resolution 11 m, inline horizontal resolution 30 m, and crossline horizontal resolution 37.5 m. Compared to amplitude data, the SI seismic with 10 - 90 Hz band pass filter data has just under 1/2 of the wavelength and vertical resolution.

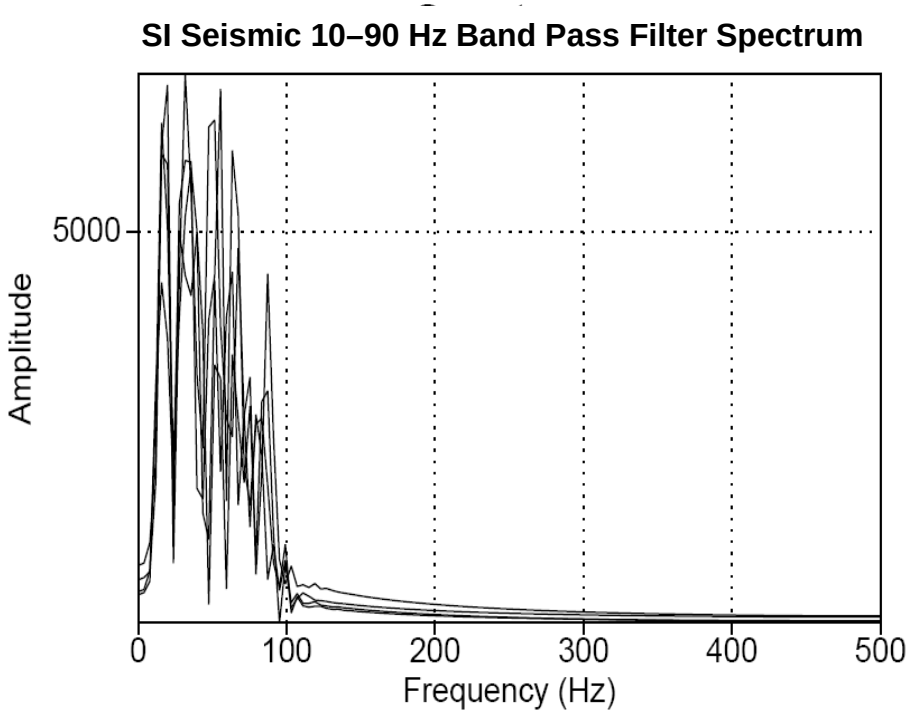

Figure 15: Frequency spectrum of SI seismic with 10 – 90 Hz band pass filter. Most energy is concentrated between 10 and 90 Hz. Nyquist frequqency is the upper limit on the x-axis.

Perov (2009) interpreted crossline 987 using seismic amplitude. The newly created SI seismic is interpreted in Figure 16. A comparison shows that both SI and amplitude seismic found a large growth fault in the middle with smaller faults on the outskirts. Most fault locations are altered including opposing fault orientations in the eastern portion of the interval. The SI seismic image shows a stronger correlation of reflectors and allows single reflections to be interpreted throughout the cross-section. This dip line section and the presence of spatial aliasing proves that interpreting this orientation is unreliable and not much improved from previous results.

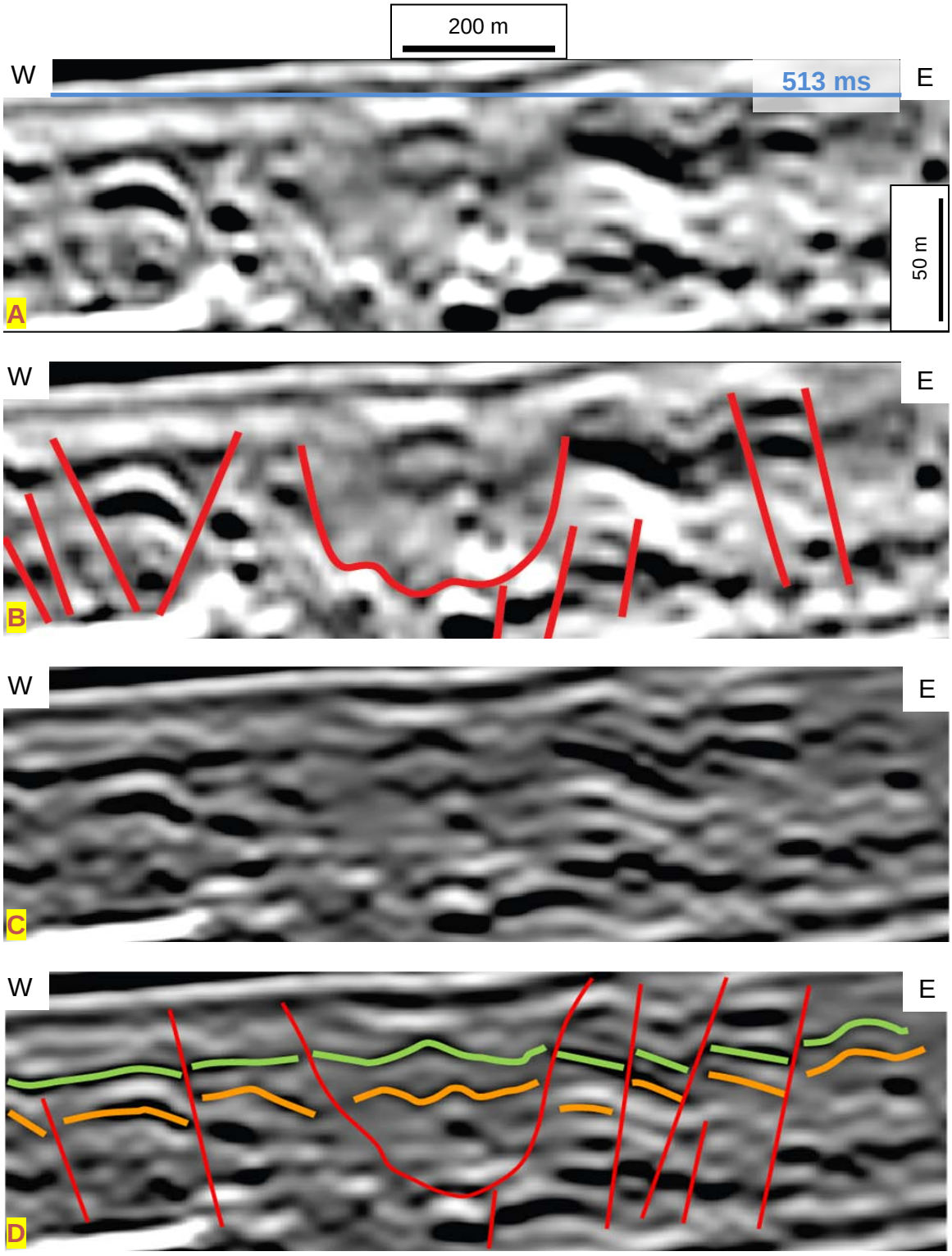

Figure 16: A) Crossline 987 seismic amplitude. B) Interpreted seismic amplitude (Taken from Perov, 2009). C) Crossline 987 in SI seismic with 10-90 Hz band pass filter. D) Interpreted SI seismic, faults in red and correlating seismic reflections in orange and green.

Perov (2009) also interpreted intersecting inline 23364 using amplitude. A cross-section of inline 23364 is shown in Figure 17. The amplitude seismic that Perov used to make his interpretation is seen in Figures 17A and B. SI seismic and an interpretation of the new image is seen in Figures 17C and D. The overall growth fault pattern is similar to Perov's interpretation, but locations of several faults and beds change. By eliminating many of the bright amplitudes and resolving thinner beds, the listric growth faults can be more clearly seen attaching to a décollement surface. However, these interpretations are not much better as the accuracy of these interpretations cannot be confirmed due to false dips and miscorrelated events that come with spatial aliasing. The clearest unaliased improvement shows vertical extension faults in the lower section of the interval. The clinoforms above and below the interval are more clearly defined as well.

Figure 18 is a closeup view of a small area within the inline 23364 chaotic interval. It shows spatial aliasing and exhibits the "string of pearls" effect so common with this problem (Liner, 2004). The dip protractor seen in Figure 18 also applies to the interpretation of this interval seen in Figure 17. Even though strike lines are better for interpretation, spatial aliasing still exists and is even worse in this orientation. Vertical exaggeration is 8:1, maximum seismic amplitude unaliased dip is 11^{o}, and maximum SI unaliased dip is 7^{o}.

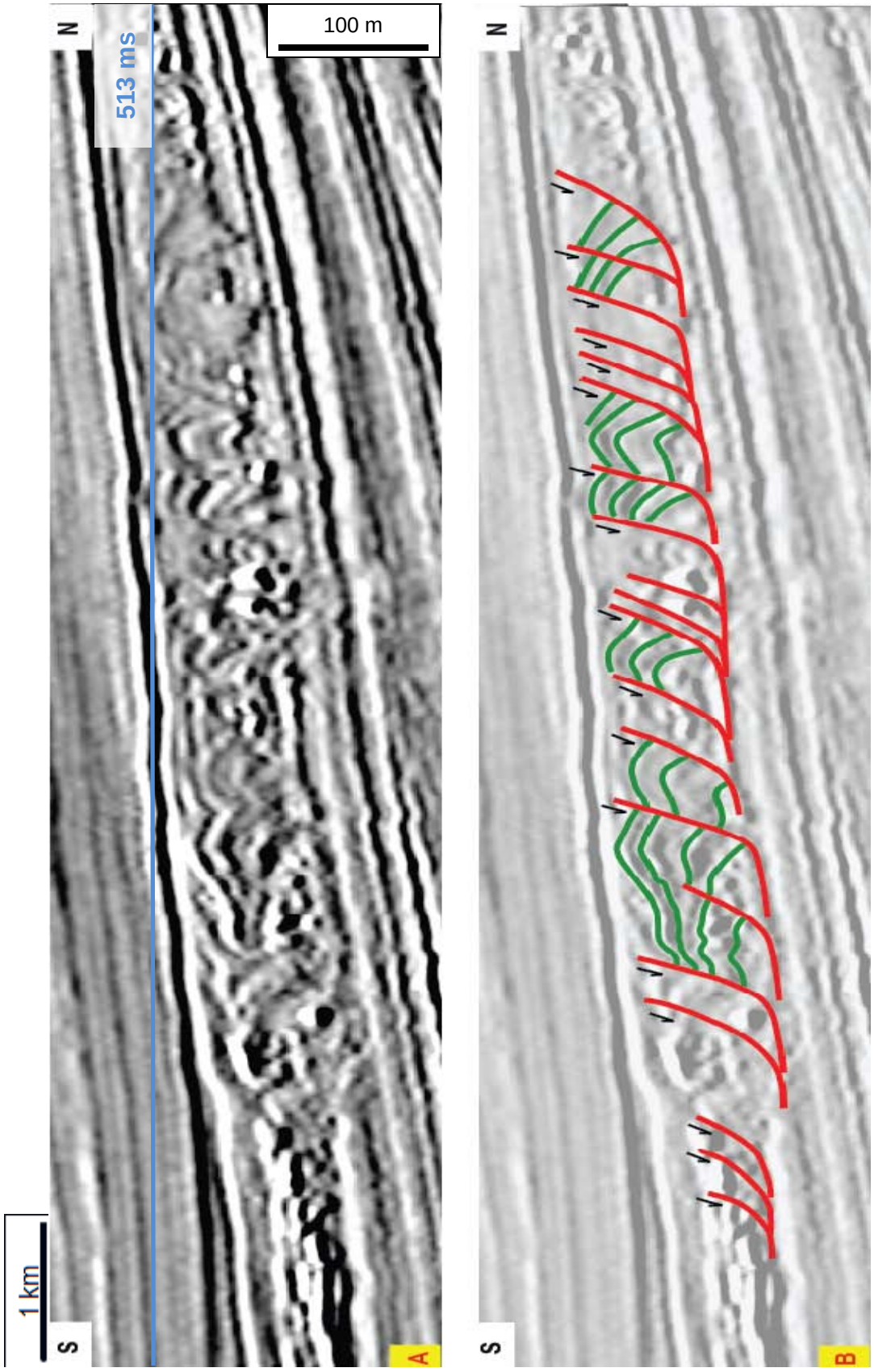
N
513 ms
100 m
1 km
S
A
N
S
B

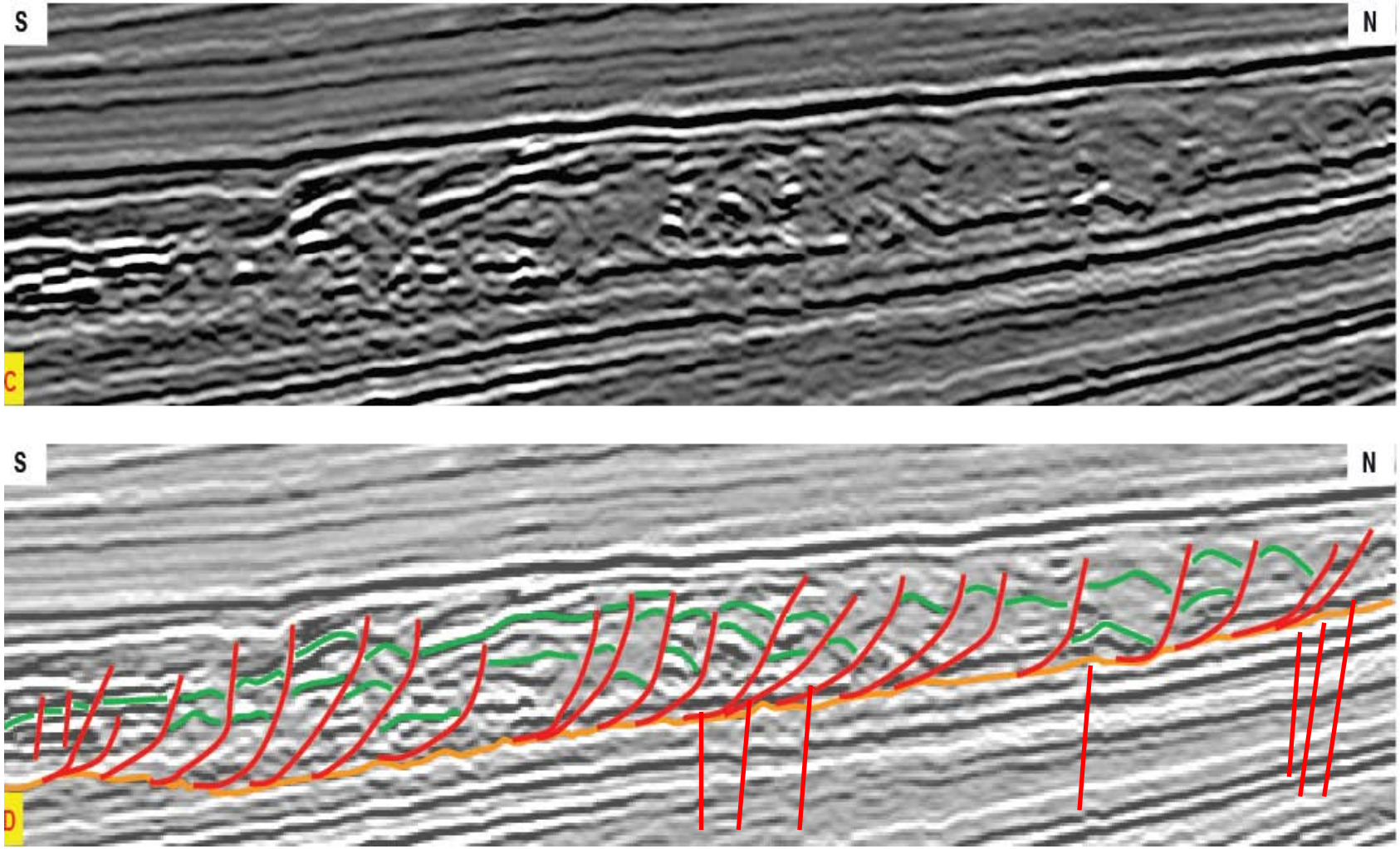

Figure 17: A)Inline 23364 in amplitude seismic. B) Interpreted amplitude seismic (Taken from Perov, 2009). C) SI Seismic with 10-90 Hz band pass filter. D) Interpreted SI seismic, growth faults in red, décollement surface in orange, and correlating seismic reflections in green.

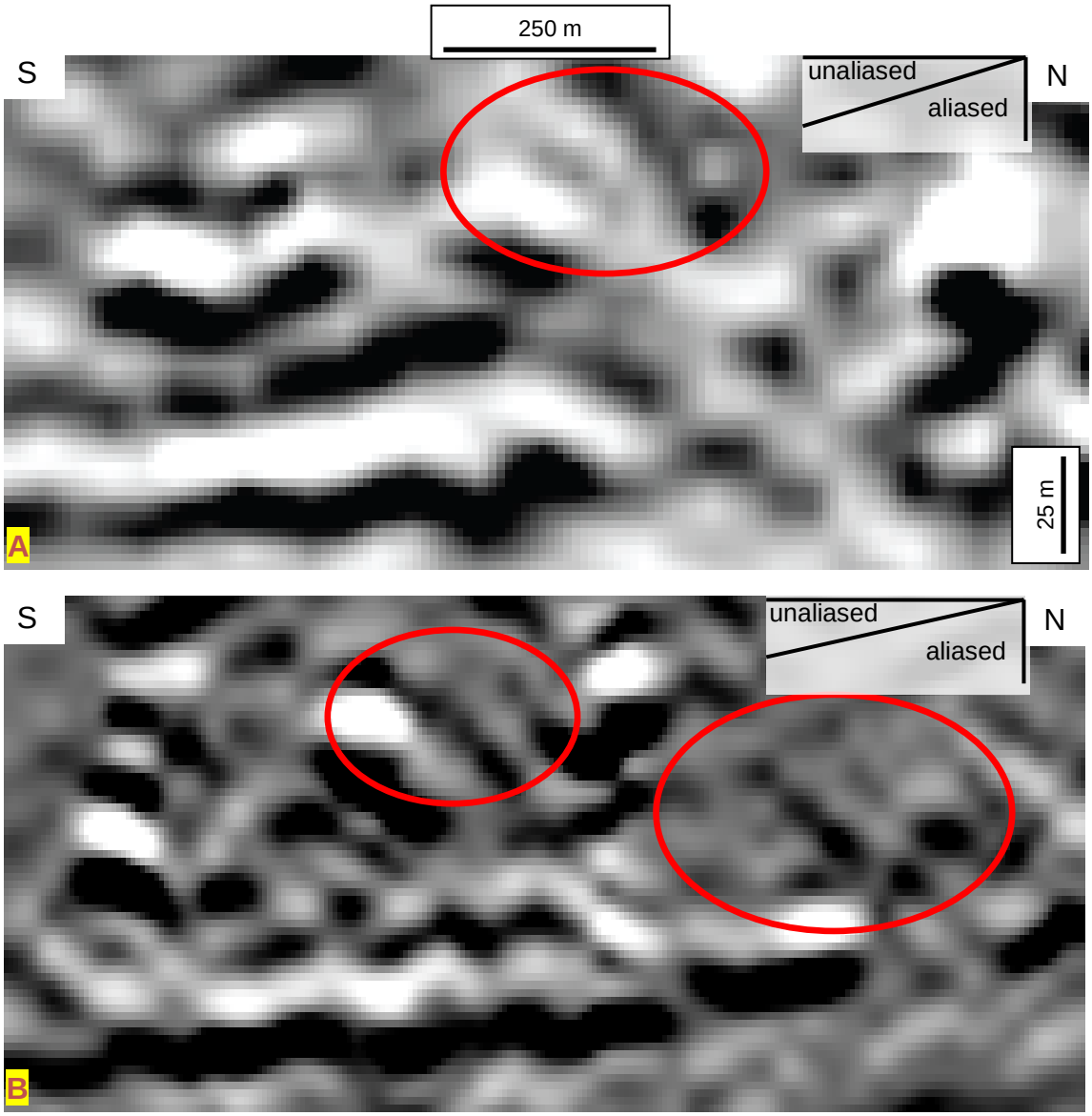

Figure 18: A) Inline 23364 seismic amplitude closeup, red circle shows “string of pearls” effect. B) Inline 23364 SI closeup, red circle shows “string of pearls” effect. Vertical exaggeration is 8:1, max amplitude unaliased dip is 11^{o}, max SI unaliased dip is 7^{o}, and dip protractor shows aliased and unaliased dips.

Perov (2009) measured growth faults seen in Figure 17, finding that spacing of faults varied from 100 m - 500 m, heights ranged from 12 m - 100 m, and throws were approximately 10 m. Incorporating the phase shift and new velocity data, we see that the growth faults display spacing from 98 m – 650 m, heights range from 15 m - 118 m. The throw of the faults remains on the order of 10 m. A comparative table can be seen in Table 2.

Perov (2009) fault measurements	**Spacing**	**Heights**	**Throw**
	100 – 500 m	12 – 100 m	~ 10 m
Phase Shift fault measurements	**Spacing**	**Heights**	**Throw**
	98 – 650 m	15 – 118 m	~ 10 m

Table 2: Comparative results of Perov's interpreted growth faults seen in Figure 17B.

Figure 19 shows a map view projection of a 513 ms time slice at the intersection of crossline 987 and inline 23364. Perov (2009) presents Figures 19A and B to support the interpretation of a large growth fault seen in crossline 987 (Figure16), evidenced by three arching faults in amplitude seismic. Seismic curvature seen in Figures 19C and D only shows one solitary arching feature surrounded by chaotic signals and acquisition footprint (Liner, 2004).

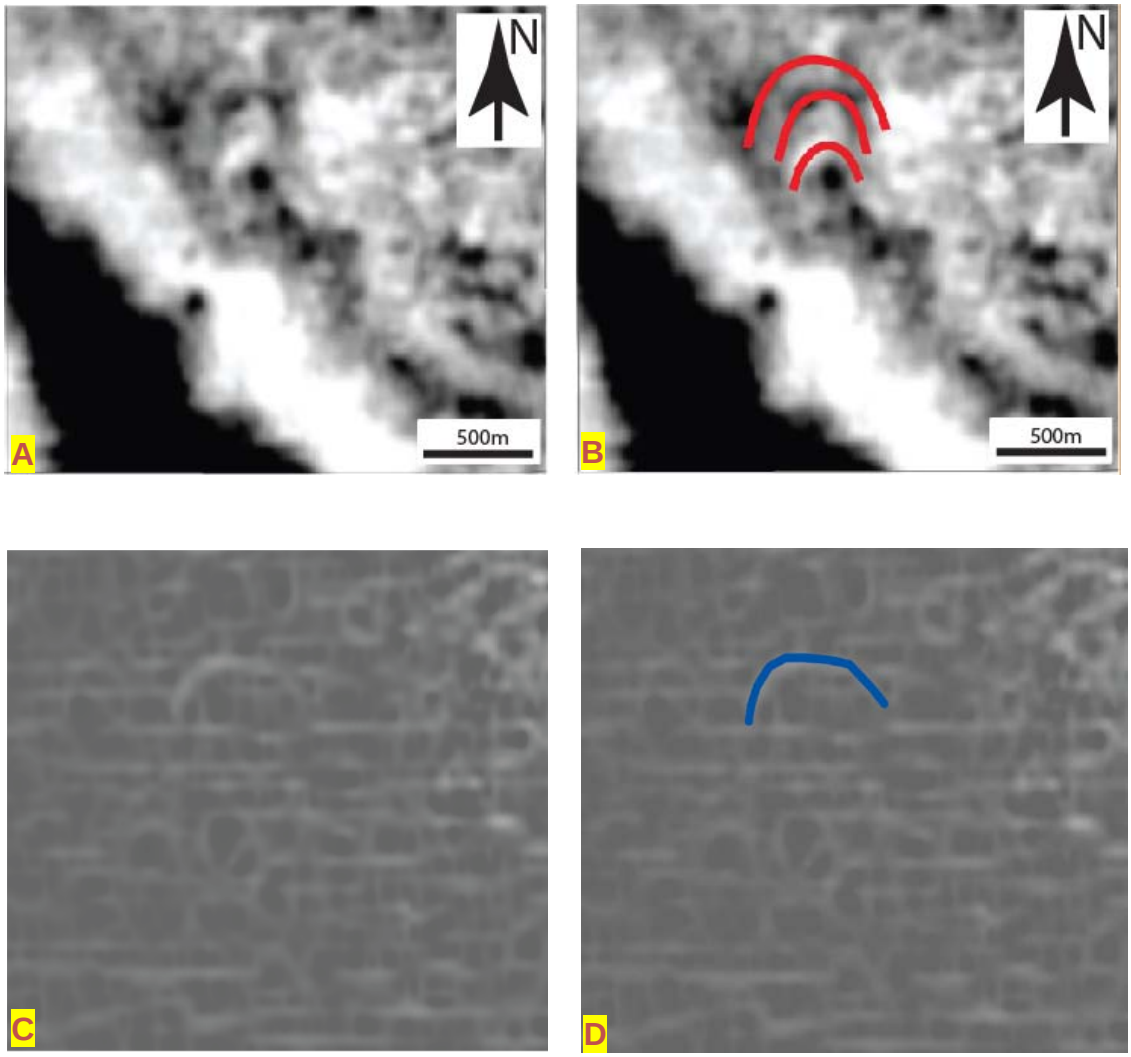

Figure 19: A) 513 ms time slice of seismic amplitude. B) Interpreted growth faults in seismic amplitude (Taken from Perov, 2009). C) 513 ms time slice of seismic curvature. D) Interpreted growth fault in seismic curvature.

Figures 19D and Figure 16D are aligned to determine if the growth fault seen in both images is the same feature. The resulting image is seen in Figure 20, which shows a correlation linking the two features in both map and cross-section view. The faint feature in curvature seismic matches fairly well with the cross-section interpretation.

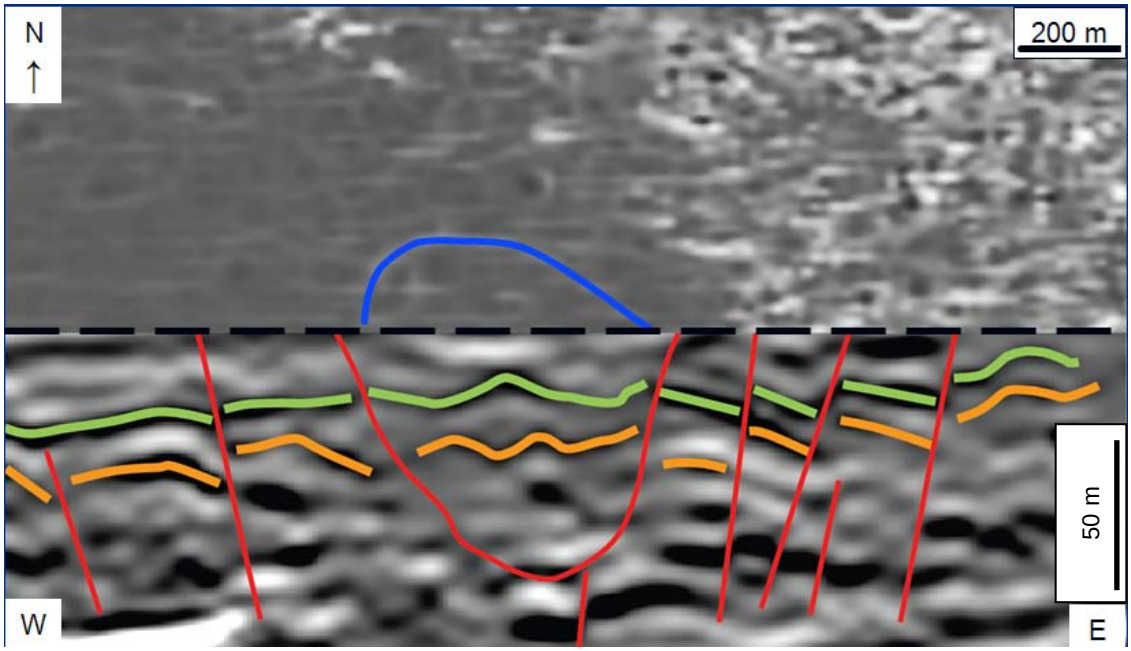

Figure 20: 513 ms time slice of curvature seismic is shown above the dashed line with interpreted SI seismic crossline 987 below. Blue fault interpretation in map view aligns with the growth fault interpretation made in cross-section.

It is important to define the shelf edge to draw conclusions about the delta environment. Perov defined this boundary by generating coherence seismic horizon slices that show slope channels and slumps. His results are shown in Figures 21A and B and indicate two distinct delta fronts and drainage systems. Figures 21C and D show my seismic coherence draped over a horizon slice of sequence boundary 1 defined by Perov (see Figure 3). In this image, slumps and low sinuosity channels are visible. An approximation of the two delta fronts is seen in Figure 21D with less channels and more slumps interpreted. Figures 21C and D also have an angled view of the coherence seismic, which helps to follow channels and topography through the mini-basin.

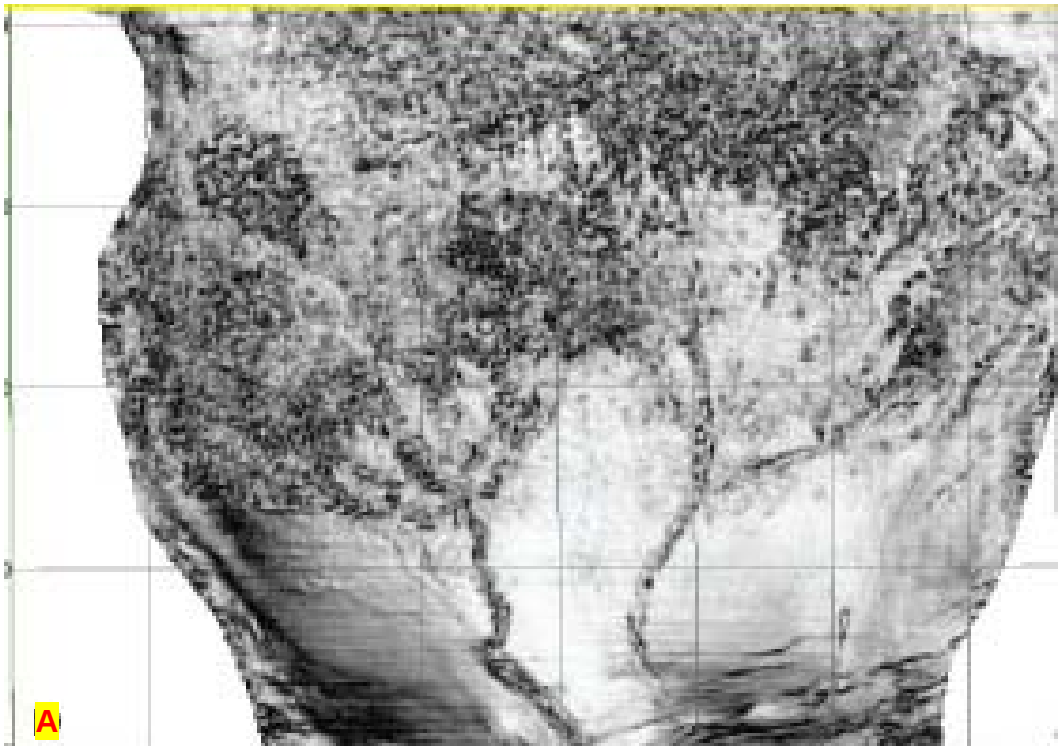
A

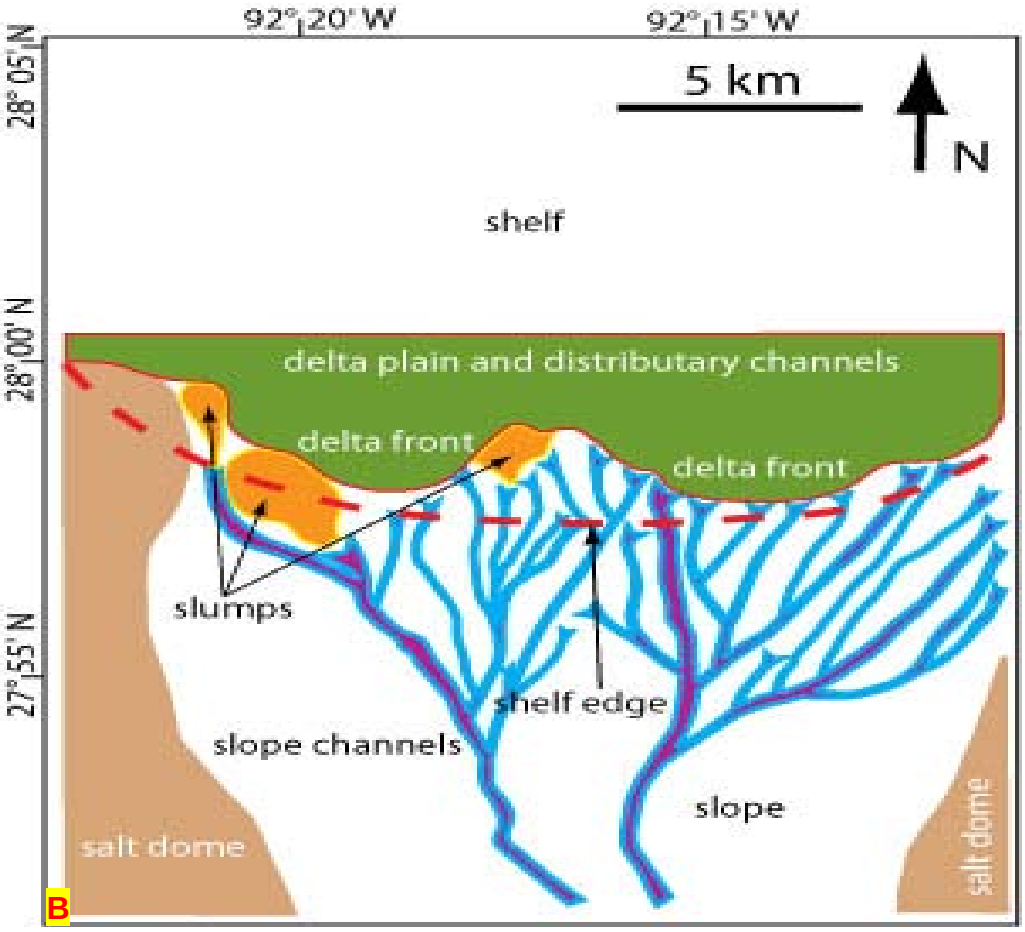
92°20' W
92°15' W
28° 05' N
28°00' N
27°55' N
5 km
N
shelf
delta plain and distributary channels
delta front
delta front
slumps
shelf edge
slope channels
slope
salt dome
salt dome
B

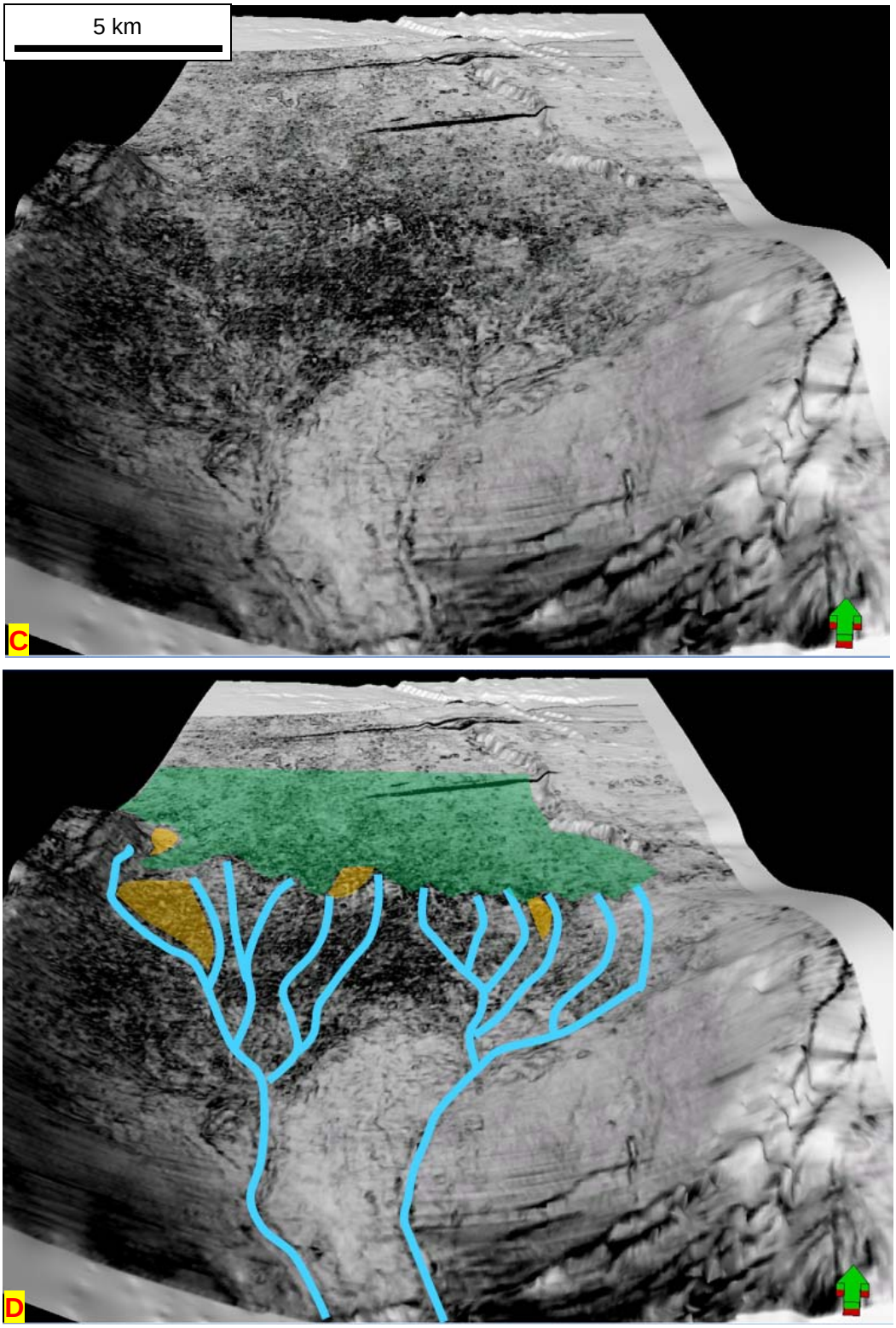

Figure 21: A) Coherence time slice. B) Interpreted coherence time slice (Taken from Perov, 2009). C) Angled view of coherence draped over sequence boundary 1. D) Interpreted coherence horizon slice, channels in blue, slumps in orange, delta fronts in green.

Perov (2009) used an amplitude seismic horizon slice to map a large mass transport complex (MTC) that occurs around 513 ms. Applying coherence and curvature to the seismic was unsuccessful in identifying this feature due to an abundance of chaotic seismic reflectors. Nevertheless, using phase shift data created earlier, the amplitude seismic was revisited. Figure 22 compares the results of Perov's amplitude seismic against phase shifted seismic amplitude. An MTC interpretation is seen in Figure 22D using the phase shifted seismic amplitude, which shows a much larger system. The phase shifted seismic amplitude tones down the bright seismic reflectors and allows interpretation of subtler pressure ridges within the MTC.

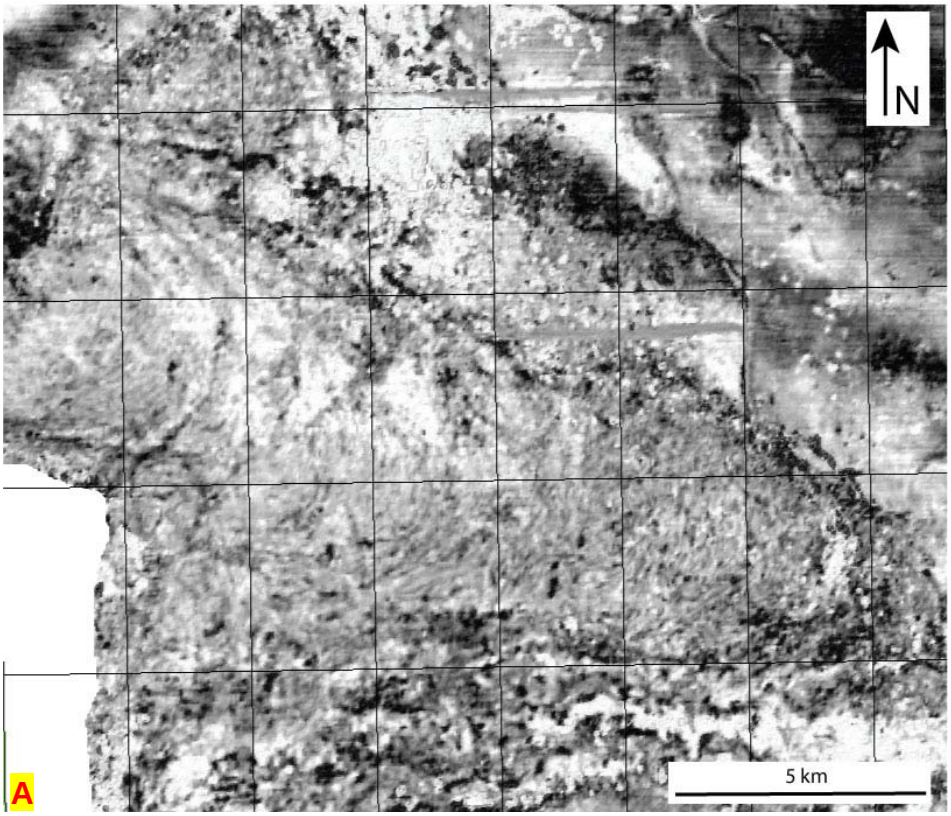
N
A
5 km

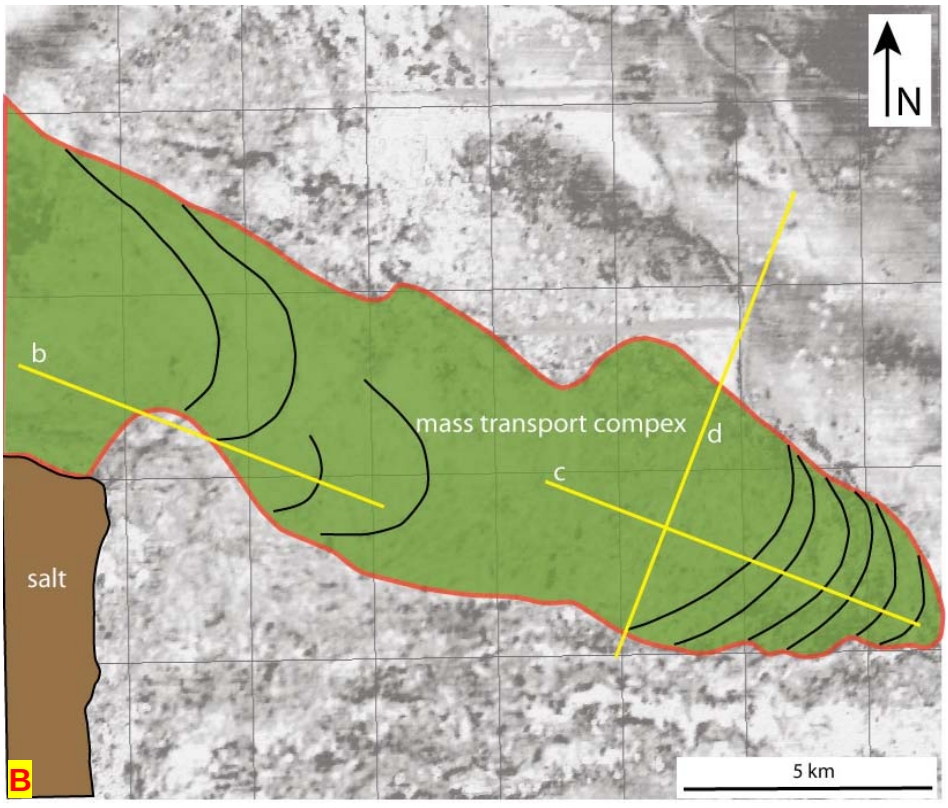
N
b
mass transport compex
d
c
salt
B
5 km

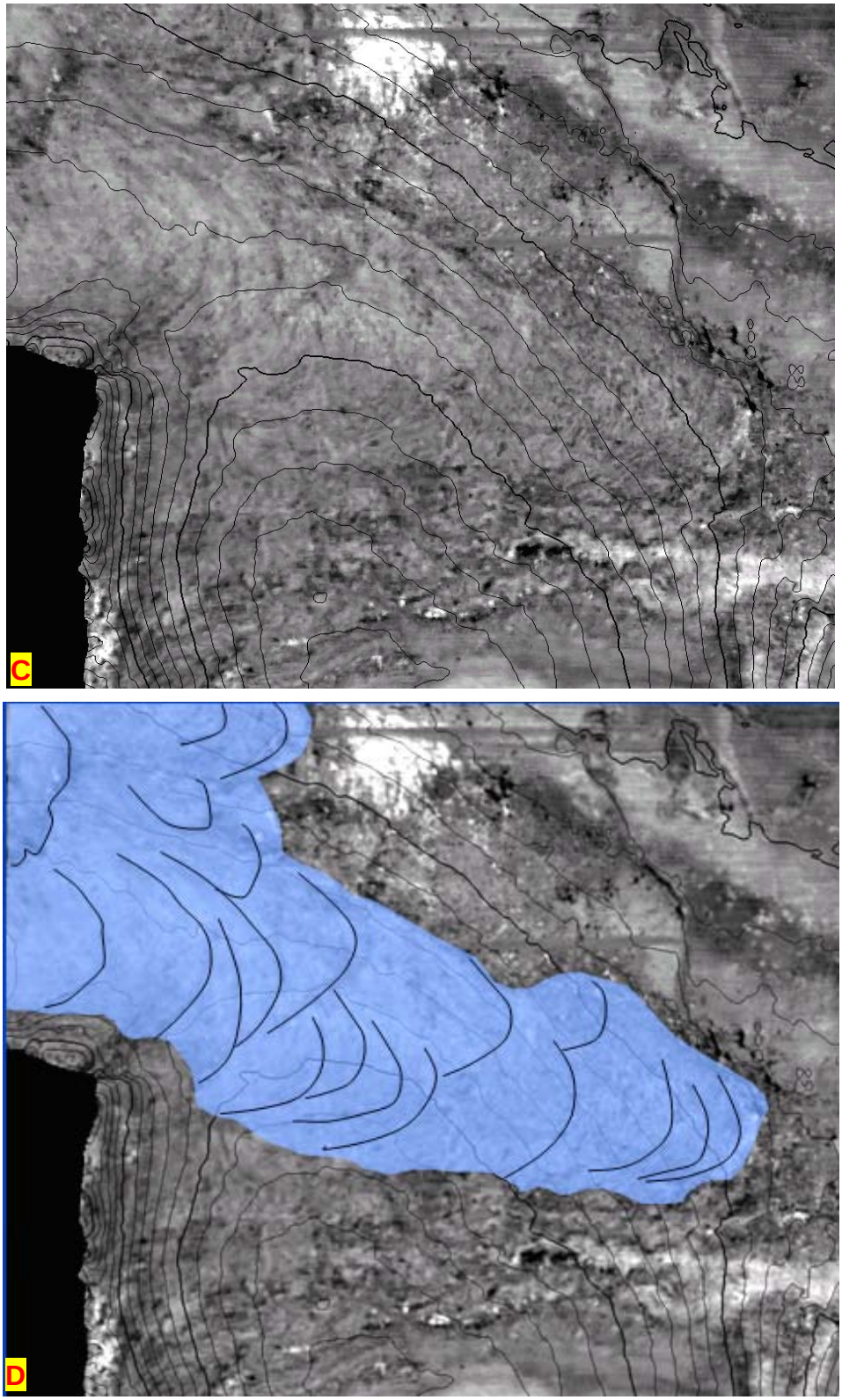

Figure 22: A) 550 ms horizon slice of amplitude seismic. B) Interpreted MTC in amplitude seismic (Taken from Perov, 2009). C) Phase shift amplitude seismic. D) Interpreted MTC in phase shift amplitude seismic, MTC in blue and pressure ridges in black. Note the handy 50 m contours.

DISCUSSION

This study uses seismic attributes to refine the location, scale, and throw of growth-faults and clinofroms as well as re-examining slope channels, slumps, and mass transport complexes (MTCs) as interpreted by Perov (2009). This study also presents a method for improving interpretability of geologic features using seismic attributes and geophysical processing to enhance seismic images.

Well check shots give accurate interval velocities and associated depths. This information changed the scale of the entire seismic dataset, which in turn affected growth fault scale and throw. Well logs allowed a phase shift correction to zero phase the seismic, which is much more precise for seismic interpretation (Widess, 1973). By achieving a balanced seismic wavelet, seismic reflectors were placed accurately within the time-depth domain.

Another result of the phase shifted seismic was improved seismic reflector clarity in seismic amplitude that allowed interpretation of an additional MTC. By eliminating an excess of negative polarity seismic reflectors, the phase shifted data allowed the interpretation of subtler positive polarity pressure ridges. Interpreted pressure ridges showed a northwest to southeast trend that is similar to previous interpretations, but the seismic now shows more pressure ridges along the northwestern border of the MTC. This links my MTC to a much larger system as described by Moscardelli and Wood (2008). This model suggests a

larger system provided sediment movement kilometers away, while gravity remobilized sediments basinward.

After applying seismic attributes, it became clear that coherence and curvature, due to smoothing and window length parameters, did not help identify growth faults, slope channels, slumps, or MTCs in cross-section. For this reason, coherence and curvature seismic only aided map view projections. Therefore, SI seismic was the primary attribute for cross-section views.

Spectral inversion seismic came in two forms, SI and SI impedance. Difficult interpretability dismissed SI impedance seismic from this study, but SI seismic showed significant improvements in resolution. After a band pass filter was applied to tie discontinuous seismic reflections, about 50% of the SI seismic resolution was lost. Resolution becomes lost as seismic reflectors grow in size merging with nearby reflectors of the same polarity. Despite the effects of band pass filtering, SI seismic resolution still improved by 6% compared to amplitude data.

While analyzing the effects of SI seismic's improved resolution, it became evident that spatial aliasing is a problem in cross-section that limits accurate interpretation in both seismic amplitude and seismic attribute data. The acquisition geometry of this data leads to a natural bin size tuned to deep targets around 5 seconds, which hinders the use of seismic attributes in these shallow seismic intervals, especially resolution enhancing attributes like SI. SI adds higher frequencies to create more seismic reflections within an interval, but this also forces dip moveout between adjacent traces to become even greater, further

spatial aliasing the data. Because seismic amplitude is lower frequency data, it can actually correlate trace-to-trace better than SI.

The frequency spectrum, interval velocity, and acquisition details highlight the fact that the data is spatially aliased in some areas. By neglecting this problem, Perov as well as this study has made some false interpretations. The false interpretations occur in the cross-section views when correlating dips that are aliased. However, there are shallow dipping features within this complex chaotic seismic interval and the surrounding clinoforms that are precisely interpreted. Despite SI having improved resolution by 6% compared to seismic amplitude, seismic amplitude has a broader range of unaliased dip detection. Therefore, SI should be used sparingly in chaotic intervals and steep dipping features should be analyzed in seismic amplitude.

The seismic coherence attribute was limited only to map view projections. Because previous interpretations already used the coherence attribute to interpret some geologic features, it did not have as great an impact as expected. Displaying coherence seismic in horizon slice showed that previous interpretations of slope channels, slumps, and delta fronts were for the most part accurate. This attribute also showed how abundant the deformation is in the area as the chaotic signals hindered precise interpretations.

The curvature seismic attribute also was limited in its ability to improve seismic interpretation due to the severe deformation in this deltaic sequence. It was applied in time slice and did help identify one growth fault. The attribute was

able to identify this growth fault due to the fault's large size, which set it apart from other neighbouring noisy reflections.

Growth Faults

A goal of this study was to determine the type and location of faults found in deltaic sequences. Many of the fault locations deviated from previous interpretations. This included the identification of nine new faults and relocation of twelve previously interpreted faults. The scale and throw of these features changed as well with better velocity and depth measurements. SI seismic provided higher resolution of these deltaic sequences allowing the listric nature and angled bedding to be identified. These SI interpreted results were taken apprehensively as miscorrelation of seismic events is possible with the steep dip of the angled beds.

Slope Channels and Shelf Edge

Coherence was used in determining the placement of slope channels and delta fronts. However, heavy noise in the slope channel interval made interpretation difficult. The chaotic seismic signal is believed to be a combination of slope channels, MTCs, and shelf margin faulting.

I was able to view 3D coherence horizon slices at different angles, and corroborate previous predictions of the shelf edge margin. I determined that previous mapping of two independent delta fronts and their successive slope channels was extremely accurate. There remains some question about the exact location of some smaller channels in the proximal portion of the delta fronts due

to incoherent seismic. Still, delta front shapes and slope channel patterns verify the interpretation of two separate delta fronts in a river dominated depositional system. Interpretation of an additional slump feature in the eastern delta front shows that the shelf edge prediction is accurate. Modification of two slumps in the western delta front shows that this delta front could advance forward as much as 250-500 m in some areas.

CONCLUSION

This study focused on extended 3D seismic interpretation using attributes to gain better understanding of geologic features. The goal was to test whether geologic interpretation could be improved by applying seismic attributes. I find that attributes can help further define geologic features in this Gulf of Mexico mini-basin. Individually, the attributes highlighted different aspects of the data, but used together, they were effective in increasing my ability to interpret subtle features. Although my results modify some details from previous interpretations, they do not drastically change previous interpretations of the development, geomorphology, or depositional system in the mini-basin.

Well data, including check shots, helped to determine correct interval velocities, depth measurements, and seismic phase in local intervals. These observations were helpful in correcting the data to zero phase.

Zero phase seismic helped show an additional mass transport complex linked to a much larger system. This indicates that the cause previously described is inaccurate. This MTC was believed to be a result of the western salt dome uplift. It now seems that the MTC is just a finger off of a much larger system originating outside the dataset's boundaries.

In this dataset, spectral inversion was able to increase cross-section resolution about 6% compared to seismic amplitude, helping determine fault locations and type. This would aid any interpretation that focuses on small-scale

growth faulting, because it increases visibility and allows an accurate measurement of distance.

Interpreters should be cautious when analyzing resolution improving attributes like spectral inversion at shallow depths as it enhances spatial aliasing. This in turn corrupts the interpretation process and causes false dips to appear in the data.

Coherence and curvature were only used in map view projections to illuminate growth faults and slope channels. Both attributes have difficulty highlighting features in a chaotic seismic interval due to the high amount of discontinuous reflections.

Complex chaotic intervals within this mini-basin cannot be accurately interpreted due to spatial aliasing. This effect destroys seismic resolution in complex intervals and aliased dips should not be interpreted as actual events. Seismic events within the unaliased zone are the only events that can be correctly interpreted.

REFERENCES

Al-Dossary, S., and K. J. Marfurt, 2006, 3D volumetric multispectral estimates of reflector curvature and rotation. Geophysics v. 71, no. 5, p. P41-P51

Bahorich, M. S., and S. L. Farmer, 1995, 3-D seismic discontinuity for faults and stratigraphic features: the coherence cube.The Leading Edge, v. 14, p. 1053-1058

Bhattacharya, J. P., 2006, Deltas, in Posamentier, H., and Walker, R.G., eds., Facies Models Revisited: SEPM, Special Publication 84, p. 237-292

Bhattacharya, J. P., and R. K. Davies, 2004, Sedimentology and structure of growth faults at the base of the Ferron sandstone member along Muddy Creek, Utah, in Chidsey, T.C., Adams, R.D., and Morris, T.H., eds., The fluvial-deltaic Ferron Sandstone: Regional-to-wellbore-scale outcrop analog studies and applications to reservoir modeling: AAPG, Studies in Geology, 50, p. 279-304

Chopra, S., 2002, Coherence cube and beyond. First Break v. 20, p. 27-33

Chopra, S., and K. J. Marfurt, 2005, Seismic attributes – a historical perspective. Geophysics v. 70 No. 5, p. 3SO-28SO

Chopra, S., and K. J. Marfurt, 2006, Seismic attributes – a promising aid for geologic prediction. CSEG Recorder, Special Edition, p. 110-121

Diegel, F. A., J. F. Karlo, D. C. Schuster, R. C. Shoup, and P. R. Tauvers, 1995, Cenozoic structural evolution and tectono-stratigraphic framework of the northern Gulf Coast continental margin, *in* M. P. A. Jackson, D. G. Roberts, and S. Snelson, eds., Salt tectonics: a global perspective: AAPG Memoir 65, p. 109–151.

Ewing, M., D. B. Ericson, and B. C. Heezen, 1958, Sediments and topography of the Gulf of Mexico. *in* E. Weeks (ed.) Habitat of Oil. AAPG Bulletin, p. 995-1053

Fahmy, W. A., G. Matteucci, D. Butters, J. Zhang, and J. Castagna, 2005, Successful application of spectral decomposition technology toward drilling of a key offshore development well: 75th Annual International Meeting, Society of Exploration Geophysicists Expanded Abstracts, 262-264

Fliedner, M. M., S. Crawley, D. Bevc, A. M. Popovici, and B. Biondi, 2002, Velocity model building by wavefield-continuation imaging in the deepwater Gulf of Mexico, Geophysics, The Leading Edge, p. 1232-1236

Galloway, W. E., 1975, Process framework for describing the morphologic and stratigraphic evolution of deltaic depositional systems, *in* Broussard, M.L., ed., Deltas; Models for Exploration: Houston Geological Society: Houston, p.87-98

Galloway, W. E., P. E. Ganey-Curry, X. Li, and R. T. Buffler, 2000, Cenozoic depositional history of the Gulf of Mexico basin: AAPG Bulletin, v. 84, no. 11, p. 1743-1774

Hilterman, F., Personal e-mail communication, 2010

Imbrie, J., J. D. Hays, and D. G. Martinson, 1984, The orbital theory of Pleistocene climate: Support from a revised chronology of the marine oxygen isotope record, *in* Berger, A.L., ed., Milankovitch and Climate: Dordecht, The Netherlands, Reidel Publishing Company, p. 269-305

Liner, Christopher L., 2004, Elements of 3D Seismology: Second Edition. PennWell: Tulsa, Oklahoma

Moscardelli, L., and L. Wood, 2008, New classification system for mass transport complexes in offshore Trinidad. Basin Research V. 20, p. 73–98

Ostermeier, R. M., J. H. Pelletier, C. D. Winker, J. W. Nicholson, F. H. Rambow, and K. M. Cowan, 2002, Dealing with shallow-water flow in the deepwater Gulf of Mexico. The Leading Edge, v. 21, p. 660-668

Partyka, G., J. Gridley, and J. Lopez, 1999, Interpretational applications of spectral decomposition in reservoir characterization: The Leading Edge, 18, 353-360.

Perov, Grigoriy, 2009, Pleistocene shelf-margin delta: Intradeltaic deformation and sediment bypass, northern Gulf of Mexico, Gulf Coast Association of Geological Societies Transactions, v. 59, p. 603

Porębski, S.J., and R. J. Steel, 2006, Deltas and sea level change: Journal of Sedimentary Research, V. 76, p. 390-403

Puryear, C. I., and J. P. Castagna, 2008, Layer-thickness determination and stratigraphic interpretation using spectral inversion: Theory and application. Geophysiscs V.73 No.2, p. R37-R48

Roberts, A., 2001, Curvature attributes and their application to 3D interpreted horizons. First Break V.19 No.2, p. 85-100

Sigismondi, Mario E., and Juan C. Soldo, 2003, Curvature attributes and seismic interpretation: Case studies from Argentina basins: The Leading Edge, November issue, p. 1122-1126

Stewart, S. A., and R. Podolski, 1998, Curvature analysis of gridded geological surfaces, Geological Society, London, Special Publications V.127, p. 133-147

Suter, J. R., and H. L. Berryhill, Jr., 1985, Late Quaternary shelf-margin deltas, Northwest Gulf of Mexico: AAPG Bulletin, V. 69, p. 77-91

Van Wagoner, J. C., R. M. Mitchum, K. M. Campion, and V. D. Rahmanian, 1990, Siliciclastic sequence stratigraphy in well logs, cores, and outcrops: Tulsa, Oklahoma, American Association of Petroleum Geologists Methods in Exploration Series, No. 7, 55

Wellner, J. S., S. Sarzalejo, M. Lagoe, and J. B. Anderson, 2004, Late Quaternary stratigraphic evolution of the West Louisiana/East Texas continental shelf, in Anderson, J.B., and Fillon, R.H., eds., Late Quaternary stratigraphic evolution of the Northern Gulf of Mexico Margin: SEPM, Special Publication 79, p. 217-235

Widess, M. B., 1973, How thin is a thin bed?: Geophysics, Vol. 38, No. 6, p. 1176-1180

Winker, C. D, 1982, Cenozoic shelf margins, Northwestern Gulf of Mexico, in Transactions—Gulf Coast Association of Geological Societies, V. 32, p. 427-448